Magnetic Field Properties inside the Jet of Mrk 421

Multiwavelength Polarimetry Including the Imaging X-ray Polarimetry Explorer

Dawoon E. Kim[1, 2, 3] ⋆, Laura Di Gesu[4], Ioannis Liodakis[5], Alan P. Marscher[6], Svetlana G. Jorstad[6, 7], Riccardo Middei[8, 9], Herman L. Marshall[10], Luigi Pacciani[1], Iván Agudo[11], Fabrizio Tavecchio[12], Nicolò Cibrario[13, 14], Stefano Tugliani[13], Raffaella Bonino[14, 13], Michela Negro[15, 16, 17], Simonetta Puccetti[8], Francesco Tombesi[3, 18, 19], Enrico Costa[1], Immacolata Donnarumma[4], Paolo Soffitta[1], Tsunefumi Mizuno[20], Yasushi Fukazawa[21, 20, 22], Koji S. Kawabata[21, 20, 22], Tatsuya Nakaoka[20], Makoto Uemura[21, 20, 22], Ryo Imazawa[21], Mahito Sasada[23], Hiroshi Akitaya[24], Francisco Josè Aceituno[11], Giacomo Bonnoli[12, 11], Vìctor Casanova[11], Ioannis Myserlis[25, 26], Albrecht Sievers[25], Emmanouil Angelakis[27], Alexander Kraus[26], Whee Yeon Cheong[28, 29], Hyeon-Woo Jeong[28, 29], Sincheol Kang[28], Sang-Hyun Kim[28, 29], Sang-Sung Lee[28, 29], Beatriz Agìs-Gonzàlez[11], Alfredo Sota[11], Juan Escudero[11], Mark Gurwell[30], Garrett K. Keating[30], Ramprasad Rao[30], Pouya M. Kouch[5, 31], Elina Lindfors[5], Ioakeim G. Bourbah[32], Sebastian Kiehlmann[33, 32], Evangelos Kontopodis[32], Nikos Mandarakas[33, 32], Stylianos Romanopoulos[33, 32], Raphael Skalidis[34, 33, 32], Anna Vervelaki[32], Sergey S. Savchenko[7, 35, 36], Lucio A. Antonelli[9, 8], Matteo Bachetti[37], Luca Baldini[38, 39], Wayne H. Baumgartner[40], Ronaldo Bellazzini[38], Stefano Bianchi[41], Stephen D. Bongiorno[40], Alessandro Brez[38], Niccolò Bucciantini[42, 43, 44], Fiamma Capitanio[1], Simone Castellano[38], Elisabetta Cavazzuti[4], Chien-Ting Chen[45], Stefano Ciprini[18, 8], Alessandra De Rosa[1], Ettore Del Monte[1], Niccolò Di Lalla[46], Alessandro Di Marco[1], Victor Doroshenko[47], Michal Dovčiak[48], Steven R. Ehlert[40], Teruaki Enoto[49], Yuri Evangelista[1], Sergio Fabiani[1], Riccardo Ferrazzoli[1], Javier A. Garcia[50], Shuichi Gunji[51], Kiyoshi Hayashida[52], Jeremy Heyl[53], Wataru Iwakiri[54], Philip Kaaret[40], Vladimir Karas[48], Fabian Kislat[55], Takao Kitaguchi[49], Jeffery J. Kolodziejczak[40], Henric Krawczynski[56], Fabio La Monaca[1], Luca Latronico[14], Simone Maldera[14], Alberto Manfreda[38], Frédéric Marin[57], Andrea Marinucci[4], Francesco Massaro[14, 13], Giorgio Matt[41], Ikuyuki Mitsuishi[58], Fabio Muleri[1], C.-Y. Ng[59], Stephen L. O'Dell[40], Nicola Omodei[46], Chiara Oppedisano[14], Alessandro Papitto[9], George G. Pavlov[60], Abel L. Peirson[46], Matteo Perri[8, 9], Melissa Pesce-Rollins[38], Pierre-Olivier Petrucci[61], Maura Pilia[37], Andrea Possenti[37], Juri Poutanen[31], Brian D. Ramsey[40], John Rankin[1], Ajay Ratheesh[1], Oliver Roberts[45], Roger W. Romani[46], Carmelo Sgrò[38], Patrick Slane[30], Gloria Spandre[38], Doug Swartz[45], Toru Tamagawa[49], Roberto Taverna[62], Yuzuru Tawara[58], Allyn F. Tennant[40], Nicholas E. Thomas[40], Alessio Trois[37], Sergey S. Tsygankov[31], Roberto Turolla[62, 63], Jacco Vink[64], Martin C. Weisskopf[40], Kinwah Wu[63], Fei Xie[65, 1], and Silvia Zane[63]

(Affiliations can be found after the references)

October 11, 2023

ABSTRACT

Aims. To probe the magnetic field geometry and particle acceleration mechanism in the relativistic jets of supermassive black holes.

Methods. We conducted a polarimetry campaign from radio to X-ray wavelengths of the high-synchrotron-peak (HSP) blazar Mrk 421, including Imaging X-ray Polarimetry Explorer (*IXPE*) measurements on 2022 December 6–8. During the *IXPE* observation, we also monitored Mrk 421 using *Swift-XRT* and obtained a single observation with *XMM-Newton* to improve the X-ray spectral analysis. The time-averaged X-ray polarization was determined consistently based on the event-by-event Stokes parameter analysis, spectropolarimetric fit, and maximum likelihood methods. We examined the polarization variability over both time and energy, the latter via analysis of *IXPE* data obtained over a time span of 7 months.

Results. We detected X-ray polarization of Mrk 421 with a degree of Π_X=14±1% and an electric-vector position angle ψ_X=107±3° in the 2–8 keV band. From the time variability analysis, we find a significant episodic variation in ψ_X. During 7 months from the first *IXPE* pointing of Mrk 421 in 2022 May, ψ_X varied across the range of 0° to 180°, while Π_X maintained similar values within ∼10–15%. Furthermore, a swing in ψ_X in 2022 June was accompanied by simultaneous spectral variations. The results of the multiwavelength polarimetry show that the X-ray polarization degree was generally ∼2–3 times greater than that at longer wavelengths, while the polarization angle fluctuated. Additionally, based on radio, infrared, and optical polarimetry, we find that rotation of ψ occurred in the opposite direction with respect to the rotation of ψ_X over longer timescales at similar epochs.

Conclusions. The polarization behavior observed across multiple wavelengths is consistent with previous *IXPE* findings for HSP blazars. This result favors the energy-stratified shock model developed to explain variable emission in relativistic jets. We consider two versions of the model, one with linear and the other with radial stratification geometry, to explain the rotation of ψ_X. The accompanying spectral variation during the ψ_X rotation can be explained by a fluctuation in the physical conditions, e.g., in the energy distribution of relativistic electrons. The opposite rotation direction of ψ between the X-ray and longer wavelength polarization accentuates the conclusion that the X-ray emitting region is spatially separated from that at longer wavelengths. Moreover, we identify a highly polarized knot of radio emission moving down the parsec-scale jet during the episode of ψ_X rotation, although it is unclear whether there is any connection between the two events.

Key words. BL Lacertae objects: HSP, –Galaxies: jets –Polarization –Relativistic processes –Magnetic fields

1. Introduction

Relativistic jets from active galactic nuclei (AGN) are the most luminous long-lived phenomena across the entire electromagnetic spectrum in the universe. This characteristic of jets makes them natural laboratories that can be studied through multiwavelength and multimessenger observations from radio to γ-rays.

Blazars are a subclass of AGN in which a relativistic plasma jet, propelled from the vicinity of a supermassive black hole, is aligned closely with our line of sight (e.g. Hovatta & Lindfors 2019). The emission from the jet is relativistically boosted toward us, and therefore dominates the spectral energy distribution (SED). The SED typically displays two broad nonthermal radiation components. The lower-frequency component is generally ascribed to be synchrotron emission from relativistic electrons. On the other hand, interpretation of the higher-frequency component falls into two different scenarios: leptonic and hadronic models. In the case of the leptonic model, the high-energy emission is attributed to Compton scattering of synchrotron photons (synchrotron self-Compton, or SSC; e.g., Jones et al. 1974; Maraschi et al. 1992) or photons from outside the jet (e.g., Dermer & Schlickeiser 1993; Sikora et al. 1994). The hadronic scenario explains the high-energy emission as proton synchrotron radiation (e.g., Aharonian 2000; Böttcher et al. 2013) or photopion production (e.g., Mannheim 1993).

Blazars are sub-classified into three different types, depending on the frequency of the synchrotron peak of the SED. Low-synchrotron-peaked blazars (LSP) have a peak frequency below 10^{14} Hz, intermediate-synchrotron peaked blazars (ISP) between 10^{14} Hz and 10^{15} Hz, and high-synchrotron peaked blazars (HSPs) above 10^{15} Hz (Abdo et al. 2010). Thus, among these subclasses, HSPs feature a synchrotron spectrum that smoothly connects from radio to X-ray bands (Fossati et al. 1998). Studies of HSPs therefore provide an opportunity to probe the geometry and dynamics of the magnetic field components present in the synchrotron emission features of the jet.

In this respect, multiwavelength polarimetry can be a prominent diagnostic tool to investigate the particle acceleration processes and the geometrical characteristics of the magnetic field inside the jet (e.g., Rybicki & Lightman 1979; Zhang 2019; Böttcher 2019; Tavecchio 2021). Until recently, polarimetric observations of blazars have been limited to optical and radio bands. However, the successful launch of the Imaging X-ray Polarimetry Explorer in late 2021 (*IXPE*; Weisskopf et al. 2022) has extended multiwavelength polarimetry up to the X-ray energy band. *IXPE* is a joint mission of NASA and the Italian Space Agency (Agenzia Spaziale Italiana, ASI). It carries three identical X-ray telescope systems (detector units; DUs) corresponding to three gas pixel detectors (GPDs, Costa et al. 2001) and three mirror module assemblies (MMAs). *IXPE* measures linear polarization in the 2–8 keV band from the photoelectric track produced by the interaction of X-ray photons and gas inside each GPD.

Mrk 421 (redshift, $z = 0.030$) is the brightest HSP blazar at X-ray energies, and therefore a prime target for measuring polarization with *IXPE* (Liodakis et al. 2019). Indeed, *IXPE* securely detected linear polarization at a level exceeding 10% during a two-day pointing of Mrk 421 in May 2022 (Di Gesu et al. 2022). In addition, during subsequent observations in June 2022, smooth rotation of the electric-vector position angle ψ_X was discovered (Di Gesu et al. 2023), in contrast to the relatively stable polarization degree and direction found for a few other HSP blazars (e.g., Liodakis et al. 2022; Middei et al. 2023). This finding can be interpreted as evidence for a helical magnetic field inside the X-ray emitting portion of the jet. Furthermore, if the X-ray emission, and therefore helical field, occurs mainly in the innermost jet, then it is expected that such rotations of ψ_X should be routinely observed. If so, X-ray observations can probe the section of the jet where the flow is accelerated and collimated (Marscher et al. 2008, 2010).

Here we report the results of a new *IXPE* observation of Mrk 421, conducted as part of a multiwavelength campaign. In §2, we present the analysis of the time-averaged data and we search for variability of the polarization properties as a function of time and photon energy. To do this, we compare the finding with the results of the previous three *IXPE* observations, and we investigate the polarization variability on long time scales. Next, in §3, we report the multiwavelength polarimetry results obtained from simultaneous and quasi-simultaneous measurements. Based on these results, we propose possible geometrical and physical interpretations of the magnetic field geometry inside the jet of Mrk 421 in §4.

2. X-ray polarization of Mrk 421

Previously, *IXPE* observed Mrk 421 three times: 2022 May 4-6 (hereafter Obs. 1), 2022 June 4–6 (Obs. 2), and 2022 June 7–9 (Obs. 3) (Di Gesu et al. 2022, 2023). Here we focus on an additional observation (Obs. ID: 02004401, Obs. 4) conducted from UTC 15:30 on 2022 December 6 to 04:00 on December 8, with a ∼ 74 ks net exposure time. During the *IXPE* pointing, Mrk 421 was in a normal X-ray activity state (e.g., Liodakis et al. 2019), with a 2–8 keV flux of ∼2×10^{-10} erg s^{-1} cm^{-2}. From this observation, we have derived the time-averaged polarization degree Π_X and electric-vector position angle ψ_X over the entire exposure. In order to investigate the X-ray polarization variability, we have also performed time- and energy-resolved analysis.

We also observed Mrk 421 with *XMM-Newton* on 2022 December 7 for 7.5 ks. In addition, the Neil Gehrels Swift Observatory (hereby referred to as *Swift-XRT*) monitored the blazar to improve the spectral and temporal coverage. Table 1 presents a summary of the X-ray observations. Detailed information on the data reduction procedures is presented in Appendix A. Throughout the manuscript, errors are given at the standard 1σ (68%) confidence level.

2.1. Time-averaged polarization properties

We have derived the linear polarization parameters from Obs. 4 by four different methods: (1) the Kislat et al. (2015) method that is implemented in the PCUBE algorithm in ixpeobssim (Baldini et al. 2022), (2) an event-based maximum likelihood method (Marshall 2021b, ML) that includes simultaneous background estimation, (3) the spectropolarimetric analysis described in Strohmayer (2017) using XSPEC, and (4) a maximum likelihood spectropolarimetric (MLS) fit implemented by the multi nest algorithm. Table 1 summarizes the Π_X and ψ_X values obtained from these methods.

First, using the Kislat et al. (2015) method, we estimated Π_X =13±2% and ψ_X =107±3° in the 2–8 keV band after background subtraction from the three combined DUs. The PCUBE measurement includes the spectral-model-independent polarization properties over a given energy and time range (Kislat et al. 2015). We derived Π_X and ψ_X from the normalized Stokes parameters Q ($\mathcal{Q} \equiv Q/I$) and U ($\mathcal{U} \equiv U/I$), according to $\Pi_X = \sqrt{(\mathcal{Q})^2 + (\mathcal{U})^2}$ and $\psi_X = 1/2 \tan^{-1}(\mathcal{U}/\mathcal{Q})$. Error estimation was calculated based on

⋆ corresponding author, dawoon.kim@inaf.it

Table 1: Results of the X-ray polarimetric and spectral observations of Mrk 421

Telescope (Method[1])	Band (keV)	Dates (YYYY-MM-DD)	X-ray Polarization Π_X(%)	ψ_X (°)	X-ray flux [2] $(10^{-10}\mathrm{erg\ s^{-1}\ cm^{-2}})$
IXPE Obs. 4 (PCUBE)	2.0 – 8.0	2022-12-06–08	13 ±2	107 ±3	–
IXPE Obs. 4 (ML)	2.0 – 8.0	2022-12-06–08	13 ±1	107 ±3	–
IXPE Obs. 4 (XSPEC)	2.0 – 8.0	2022-12-06–08	14 ±1	107 ±3	2.25 ±0.04
IXPE Obs. 4 (MLS)	2.0 – 8.0	2022-12-06–08	13 ±1	109 ±3	–
Swift-XRT	0.3 – 10.0	2022-12-06	–	–	3.20 ±0.06
XMM-Newton	0.3 – 10.0	2022-12-07	–	–	2.04 ±0.04
Swift-XRT	0.3 – 10.0	2022-12-08	–	–	2.47 ±0.05
IXPE Obs. 3 (PCUBE)	2.0 – 8.0	2022-06-07–09	10 ±1	Rotation	3.02 ±0.02
IXPE Obs. 2 (PCUBE)	2.0 – 8.0	2022-06-04–06	10 ±1	Rotation	1.57 ±0.01
IXPE Obs. 1 (PCUBE)	2.0 – 8.0	2022-05-04–06	15 ±2	35 ±4	0.87 ±0.003

Notes. [1] Methods are described in §2.1. [2] X-ray flux in the 2–8 keV band.
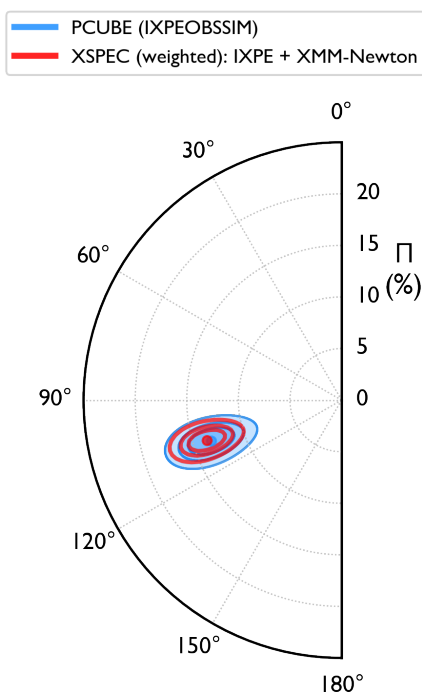
Fig. 1: Polarization contours from Obs. 4. Contours represent the significance of the time-averaged polarization detected with confidence levels of 68.27%, 90.00%, and 99.00%, with two degrees of freedom. The blue contour indicates the values of Π_X and ψ_X derived from the PCUBE methods, and the red contours show the same properties from simultaneous *IXPE* and *XMM-Newton* spectropolarimetric analysis. The radial and angular values represent Π_X and ψ_X, respectively, with the latter measured from north through east.

Kislat et al. (2015) and Muleri (2022). Figure 1 indicates the detection significance of this measurement in the form of a polarization contour plot.

The second method (ML) uses an event-based maximum likelihood method to determine Q and U (Marshall 2021b). The method accounts for background using data from an annulus about the target by including a term in the likelihood, as used in the analysis of the IXPE data of Cen A (Ehlert et al. 2022).

Source events were selected from a region of 60″ radius about the source centroid, while the background events were selected from an annulus with inner and outer radii of 200″ and 300″. In this case, Π_X = 13±1% and ψ_X =107±3°.

Next, the spectropolarimetric analysis examined the X-ray spectra and polarization properties based on spectral modeling with XSPEC (ver. 12.13.0c; Arnaud 1996). With this method, we obtained Π_X =14±1% and ψ_X =107±3°. The detection significance of this measurement was $\gtrsim 11\sigma$. The flux was estimated as 2.25 (±0.04) ×10^{-10} erg s^{-1} cm^{-2} over 2–8 keV, the same band over which the *IXPE* I, Q, and U spectra were obtained. In this analysis, we additionally included the simultaneous *XMM-Newton* data in order to refine the constraints on the spectral shape over the 0.3–10 keV energy range. The cross-calibration factors among all the spectra are accounted for using the CONSTANT model, normalized to the *XMM-Newton* spectrum while the other spectra were varied. In all the fits, we considered the Galactic absorption along the line of sight of Mrk 421. For this, we used the TBABS model with weighted average column density values from HI4PI Collaboration et al. (2016) ($N_H = 1.34 \times 10^{20}$cm^{-2}). The WILM model was applied to take into account metal abundance (Wilms et al. 2000). For the spectral modeling, we first applied a simple power law model (POWERLAW in XSPEC) to reproduce the I synchrotron spectrum, but the best-fit result was poor, with χ^2/d.o.f.=3308/651. Hence, we employed the log-parabolic model (LOGPAR), in which the photon index varies with energy following a log parabola function (Massaro et al. 2004):

$$N(E) = K(E/E_{pivot})^{(\alpha - \beta \log(E/E_{pivot}))}, \quad (1)$$

where the pivot energy E_{pivot} is a scaling factor, α describes the slope of the photon spectrum at E_{pivot}, β expresses the spectral curvature, and K denotes a normalization constant. This spectral model generally describes a typical HSP spectrum well, including that of Mrk 421, both in quiescence and in flaring states (Donnarumma et al. 2009; Baloković et al. 2016). As the photon index varies with energy in this model, the choice of reference energy E_{pivot} changes the determined value of α. In our spectral fit, we fixed the pivot energy to 5.0 keV (e.g., Baloković et al. 2016; Middei et al. 2022). In this case, the α parameter approximately corresponds to the photon index over 3.0–7.0 keV. In our spectral fitting, we also allowed the values of α, β, and K to vary. These free parameters are coupled with the reference spectrum, which here is the *XMM-Newton* PN spectrum
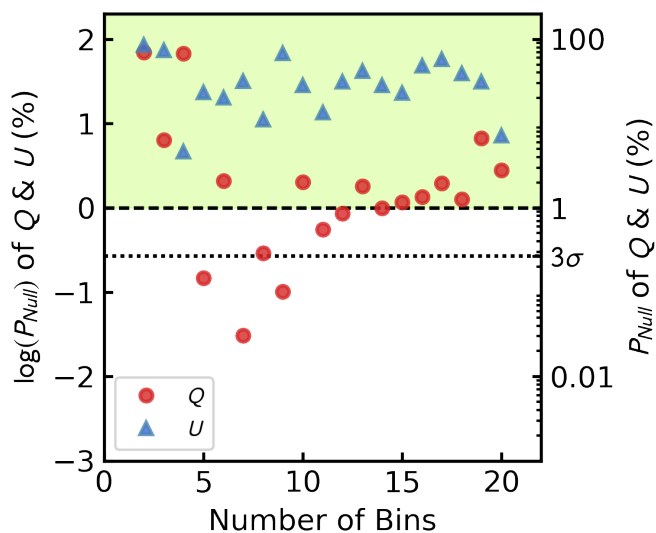
Fig. 2: The null-hypothesis probability of the χ^2 test for time variability of the Q (red) and $\mathcal{U}$ (blue) Stokes parameters with the constant model for different numbers of time bins for Obs. 4. The left and right vertical axes correspond to the probability values in logarithmic and linear scales, respectively. The green shaded area indicates that the null-hypothesis probability is above the 1% significance level. The black dashed and dotted lines located in the middle of the panel represent 1% and 3σ (99.73%) probability, respectively.

over the same 2-8 keV band to which the 3 *IXPE* DUs are sensitive. Finally, the X-ray polarimetric measurements were constrained by the `POLCONST` model based on the Stokes parameter fits. Consequently, we obtained statistically acceptable fits, with χ^2/d.o.f.=740/650, above 99% confidence level. Figure A.1 and Table A.1 present the parameter values of our best-fit results. We note that in the Stokes-spectra-decoupled case, which only fits I spectra without involving `POLCONST`, the best-fit results obtained the same values as we derived from the simultaneous spectropolarimetric fit.

Finally, the MLS method was also applied to determine the polarization properties for the `POWERLAW` spectral model. With this procedure, we derived the polarization and spectral properties to be $\Pi_X = 13\pm1\%$ and $\psi_X = 109\pm3°$.

We have thus derived that the X-ray polarization properties by four different methods are consistent within the uncertainties (see Table 1). The small differences can be explained by the fact that the `PCUBE` analysis estimated spectral-model-independent polarization properties, while the `XSPEC` methods take into account the best fit from the spectral modeling. Furthermore, among the current choices, only the `XSPEC` method can improve sensitivity by applying event weight methods introduced by Di Marco et al. (2022). Overall, we find that the Π_X and ψ_X results are robust, with modest statistical errors (see Figure 1).

2.2. Polarization variability

We have investigated whether the polarization varies as a function of time or energy. We tested the time dependence using two methods. In the first one, we determined the null-hypothesis probability with the χ^2 test using the combined `PCUBE` and `XSPEC` analysis (e.g., Di Gesu et al. 2022; Gianolli et al. 2023;
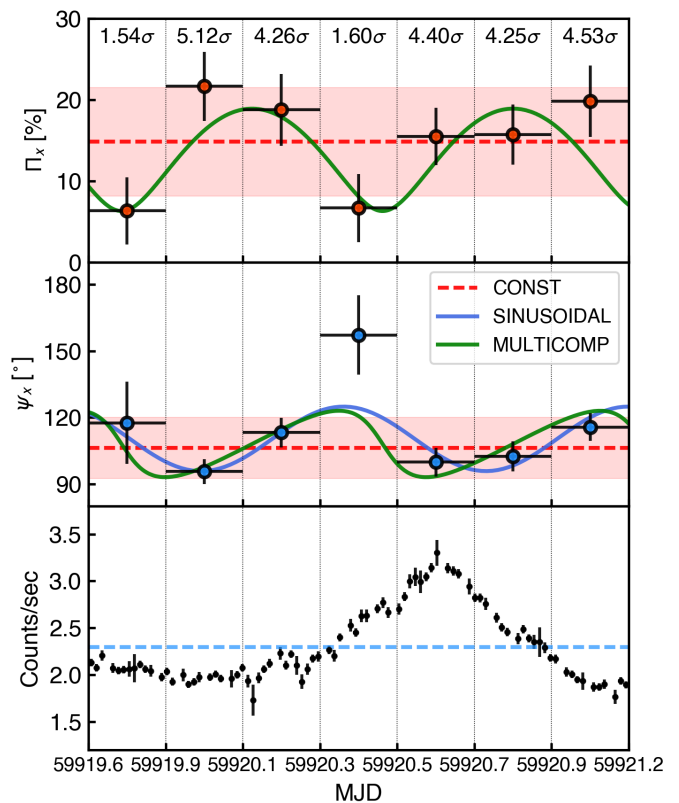
Fig. 3: *IXPE* polarization and photon counts versus time during Obs. 4. From top to bottom: Π_X, ψ_X, and count rates. Polarization results are from a time-resolved analysis with seven identical 19 ks time bins. The detection significance for each bin is displayed at the top of the figure. In Π_X and ψ_X panels, red dashed lines denote a fit to a constant function; the shaded area corresponds to $\leq 3\sigma$ uncertainty. In addition, the blue and green solid lines indicate the best-fit result with the sinusoidal and multi-component model, respectively. The blue dashed line in the light curve indicates the average value during the observation.

Di Gesu et al. 2023). For the second method, we used the unbinned event-based maximum likelihood analysis implemented in Marshall (2021a). With this method, we can avoid the error that can be caused by subjective selection bias resulting from the binning criteria.

The first method measured each normalized Stokes parameter value by dividing the data into identical time spans that depended on the selected number of bins (e.g., 2 bins= 100 ks/2 bins = 50 ks/bin). In particular, we split Obs. 4 into 2 to 20 time bins. We then compared Q and $\mathcal{U}$, which followed a Gaussian error distribution, with the results from fitting each parameter treated as constant over time (i.e., $Q(t) = Q_0$ and $\mathcal{U}(t) = \mathcal{U}_0$). The result of fitting the constant model was calibrated for each number of bins. We then calculated the χ^2 and the null-hypothesis probability (for the corresponding degrees of freedom) for each case. Figure 2 indicates the null-hypothesis probability as a function of the number of bins. In this figure, the green-shaded area ($P_{\text{Null}} > 1\%$) corresponds to cases where the data are statistically consistent with values of Q and $\mathcal{U}$ that are constant in time. Conversely, if the points lie outside the region ($P_{\text{Null}} < 1\%$), it implies that the polarization varies with time. As seen in Figure 2, we found that splitting the $Q(t)$ light curves with 5, 7, 8, 9, 11, 12, and 14 time bins does not pro-
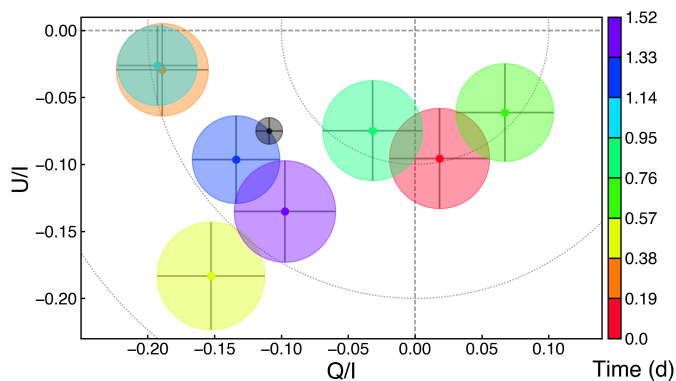
Fig. 4: The time variability of the Q and $\mathcal{U}$ Stokes parameters during Obs. 4. Each circle indicates the 1σ uncertainties of eight identical time intervals, derived using an event-based maximum likelihood technique as described in Di Gesu et al. (2023). The black circle shows the time-averaged polarization. Each color represents each time interval from the start to the end of the Obs. 4.

duce a good fit with the constant model ($P_{\text{Null}} < 1\%$). The case of 7 time bins has the smallest null-hypothesis probability, with $\chi^2/\text{d.o.f.}=25.26/6$, beyond the 3σ confidence level. In the polarization light curve of Obs. 4 with seven identical time bins (Figure 3), we can see that ψ_X varies from the second to the fourth bin, after which it returns to a more stable value near that of the first three bins. We estimate the rotation rate of this variation as $\dot{\psi} \sim 92°$/day (change by $61°$ over ~57 ks from the second to the fourth bin). This result is comparable to the rotation rate of $\dot{\psi} = 85°$/day reported in Di Gesu et al. (2023).

Additionally, in order to examine the possibility of continuous change of ψ_X, we have tested whether a sinusoidal function ($\psi_X(t)=A\sin(Ct - D) + B$) provides a better fit of $\psi_X(t)$ with respect to a constant function corresponding to the mean value of ψ_X over 7 time bins (blue line in Figure 3). This approach yielded a smaller $\chi^2/\text{d.o.f.}$ value of 4.75/3, with a Bayesian information criterion (BIC) of 12.53, than the constant model ($\chi^2/\text{d.o.f.}=16.66/6$, BIC=18.60).

As a second approach, we employed a maximum likelihood method that allows for ψ_X rotation in each interval, as described elsewhere (Di Gesu et al. 2023) and shown in Figure 4. Briefly, the ML method is used (see §2.1) for eight equal time intervals but also allowing for ψ_X rotation during the time interval, as an "uninteresting" parameter. This approach prevents ψ_X rotations during a time interval from reducing the average polarization of that interval, which is important when there are large ψ_X changes. For example, Figure 4 shows that there appear to be large, nearly $90°$ ψ_X shifts between intervals one and two and between intervals three and four. As a result, we confirmed that ψ_X varied over time during Obs. 4 with $\sim 4.5\sigma$ confidence.

In addition, with a maximum likelihood method, we tested a more complex model fit — the multicomponent model (Pacciani et al. in preparation), which involves the convolution of constant and rotating polarization components — to check the possibility of continuous variation within the Obs. 4 period. The details of this model are described in Appendix B. From this test, we computed the significance of the multicomponent model relative to the constant polarization model based on the delta likelihood, $\Delta S' = S'(\Pi_0, \Psi_0, 0) - S'(\Pi_1, \Psi_1, \Pi_2, \Psi_2, \omega)$. We obtained a decrease in the likelihood estimator, $\Delta L = -32.4$, which follows a chi-square distribution with three degrees of freedom. Hence,

Table 2: Parameters for the multicomponent model

$R_1 \cdot \Pi_1$ (%)	Ψ_1 (°)	$(1 - R_1) \cdot \Pi_2$ (%)	Ψ_2^0 (°)	ω (°/day)
12.6 ± 1.6	108 ± 4	6.3 ± 1.8	-96 ± 17	246 ± 23

the constant polarization model is rejected in favor of the multicomponent model, at the $\sim 5\sigma$ confidence level that this result occurred by chance. The parameters estimated with the multicomponent model are reported in Table 2. The observed discrepancy between the rotation rate measured from the multicomponent model (i.e., $\omega = 245°$/day) and the rate estimated directly from the light curve (i.e., $\dot{\psi} \sim92°$/day) can be explained by differences in physical interpretation. The multicomponent model assumes a persistent presence of the rotating component in conjunction with the constant emission component, while the other case assumes that the emission originates from a single dominant component. The multicomponent model is indicated with a green line in Figure 3.

Therefore, based on these different methods, we conclude that we have found an episodic ψ_X variation over time during Obs. 4. Furthermore, the results of sinusoidal and multicomponent models suggest that the variations may be attributed to continuous changes in stable components. However, due to differences in the analysis methods employed, these two models were not compared in this study. Moreover, since these model fit results were derived as relative outcomes compared to the constant model, we cannot rule out the possibility of encountering more complex components and potential stochastic variations.

We also tested whether the X-ray polarization depends on energy by applying the same null-hypothesis probability test discussed above, but with the *IXPE* energy band (2–8 keV) divided into smaller ranges. We did so for two energy bins (2–4 and 4–8 keV), as well as three energy bins (2–4, 4–6, and 6–8 keV), etc., up to 12 energy bins. We found no statistically significant differences with a constant fit, as $P_{\text{Null}} \geq 13\%$ from both Q and $\mathcal{U}$, hence the data are consistent with energy-independent X-ray polarization.

2.3. X-ray polarization and spectral variability across multiple IXPE observations

Significant X-ray polarization from Mrk 421 has been detected at four epochs with *IXPE* (see Table 1). Figure 5 shows error contours for both time-averaged and time-resolved data of each observation. Over the seven months from *IXPE* Obs. 1 to Obs. 4, the value of ψ_X varied widely, with a continuous rotation over $180°$ observed during Obs. 2 and Obs. 3. In contrast, measurements of Π_X for all events were similar within a range of 10–15%, even though the time-averaged Π_X of Obs. 2 and Obs. 3 appears to be clearly lower than in the other cases due to dilution by the changing of ψ_X. However, the mean value of Π_X during periods of nonrotation of ψ_X (Obs. 1 and Obs. 4) was $14 \pm 2\%$, a factor of 1.4 ± 0.2 higher than the value of $10 \pm 1\%$ during the rotation (Obs. 2 and Obs. 3). This result is similar to the findings of previous optical polarimetry studies: (1) Blinov et al. (2016b) observed that the ratio of Π_O of rotating to that of nonrotating cases is less than 1 in 18 out of the 27 observed rotations, and (2) Jermak et al. (2016) reported a 26% reduction in the average Π_O during rotational periods compared to nonrotational periods. Nonetheless, because of the limited amount of X-ray polarization data, this result should be verified with an in-

Time-averaged polarization contours

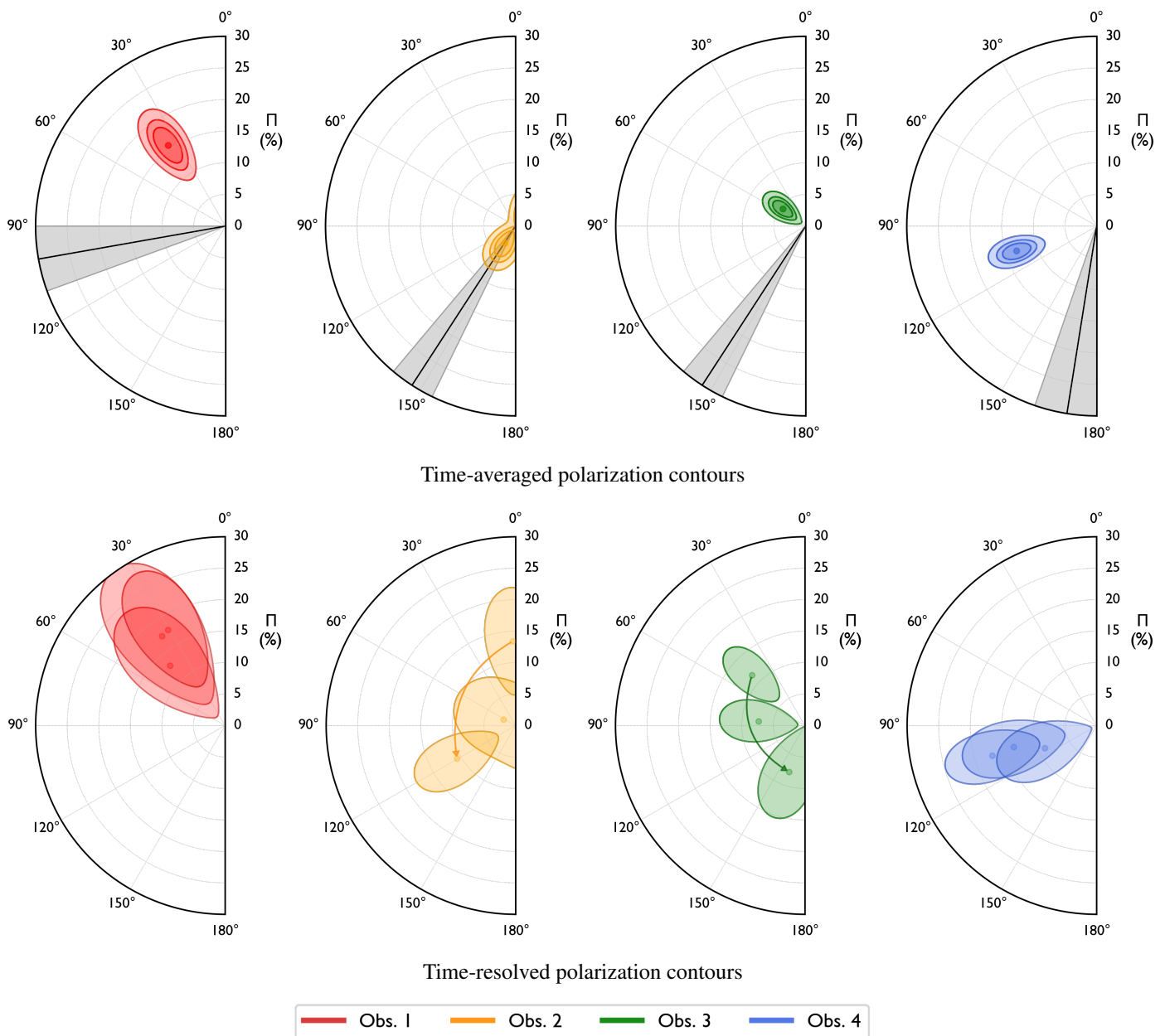Time-resolved polarization contours

Fig. 5: Time-averaged and time-resolved polarization contours of four multiple *IXPE* observations. In the top panel, each colored contour represents the significance of the time-averaged polarization detection for the corresponding observation (Obs. 1: red, Obs. 2: orange, Obs. 3: green, and Obs. 4: blue). Contours are shown at confidence levels of 68.27%, 90.00%, and 99.00%, from a χ^2 test with two degrees of freedom. Additionally, the black line and gray shaded areas indicate the jet's electric vector position angle (EVPA) in degrees as observed by the VLBA at 43 GHz (Obs. 1: 100±10°, Obs. 2: 147±7°, Obs. 3: 147±7°, and Obs. 4: 171±10°). In the bottom panel, the 99.00% confidence level contours show the time variation of polarization properties by dividing the data into three identical time intervals for each observation. In the cases of Obs. 2 (orange) and Obs. 3 (green), arrows indicate a rotation of ψ_X from the start to the end of the observation.

creased number of measurements from future X-ray polarimetry monitoring observations.

The radio electric-vector position angle ψ_{43GHz} obtained from the 43 GHz Very Long Baseline Array (VLBA) observations (black line in Figure 5) differs from ψ_X and which also changes by 70° over the 7 months from Obs. 1 to Obs. 4. The pronounced variation of ψ_X and ψ_{43GHz} contrasts with the steadier X-ray polarization observed in other sources of the same subclass of blazars, whose synchrotron SED peaks at X-ray frequencies (i.e., Mrk 501; Liodakis et al. 2022).

We have also investigated the spectral properties and X-ray activity of Mrk 421 through *Swift-XRT* monitoring observations. Figure 6 presents the α and β spectral parameters obtained from the LOGPAR model fit. We also derived the X-ray flux in the soft (0.3–2 keV), F_{soft}, and hard (2–10 keV), F_{hard}, energy bands, and define the hardness ratio as $(F_{hard} - F_{soft}) / (F_{hard} + F_{soft})$. We have found that the α parameter, representing the slope of the spectrum at the pivot energy, maintained similar values in Obs. 1 and Obs. 4. However, during Obs. 2 and Obs. 3, α decreased with time. In addition, the hardness ratio also varied during the ψ_X rotation, while its value in Obs. 1 was consistent with that in Obs.
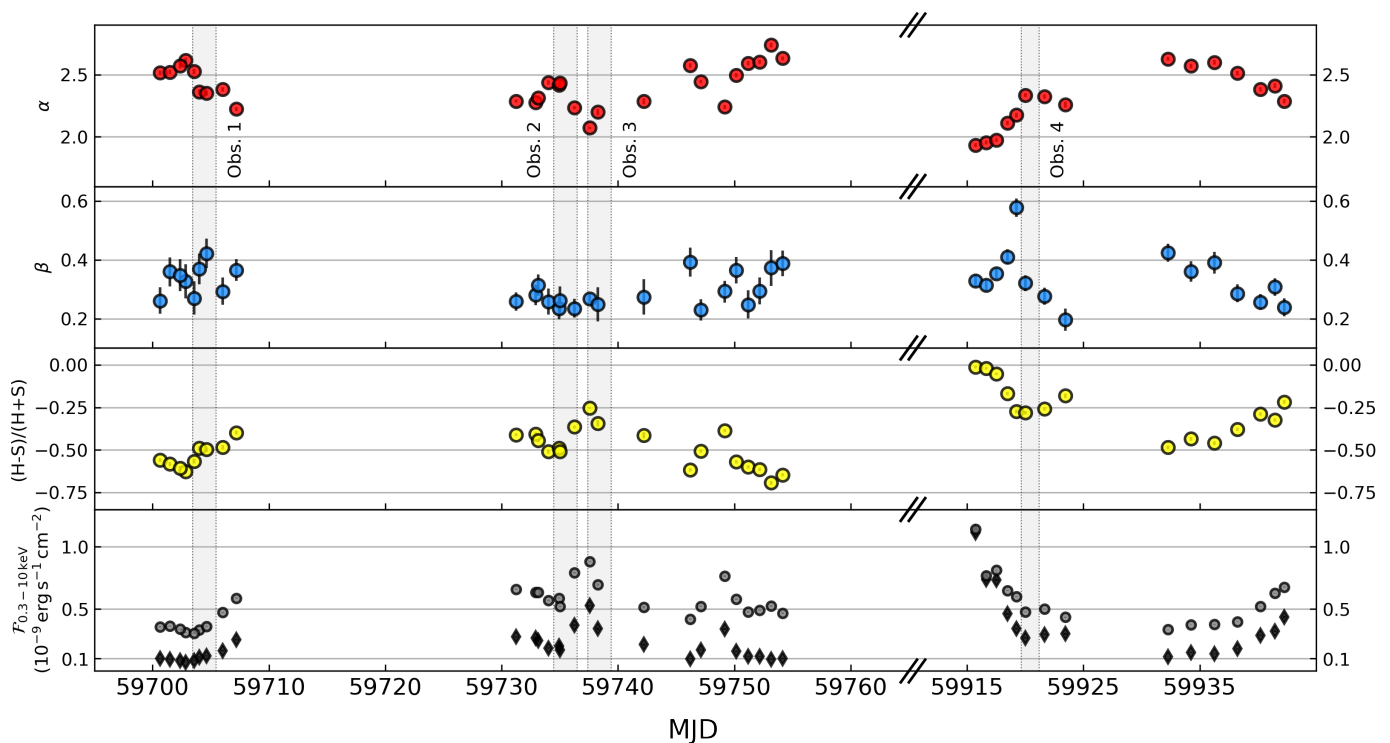
Fig. 6: *SWIFT-XRT* X-ray spectral parameters and flux versus time of Mrk 421 from a log-parabolic best-fit model with E_{pivot}=5 keV. From top to bottom: α, β, hardness ratio, and flux in the soft (0.3–2 keV, gray circles) and hard (2–10 keV, black diamonds) energy bands. The time ranges of the *IXPE* pointings are indicated by the gray-shaded regions.

4. Nonetheless, in the case of Obs. 4, *Swift-XRT* observations were conducted only at the beginning and shortly after the *IXPE* pointing, thus we cannot exclude the possibility of variations of spectral properties during Obs. 4.

The X-ray fluxes of Mrk 421 during all epochs of *IXPE* observations were within 1σ of the median historical value (e.g., Liodakis et al. 2019). Nonetheless, we found significant fluctuations during Obs. 2 and Obs. 3. Although the flux variations occurred during all of the *IXPE* epochs (see, e.g., Figure 3), the discrepancy between the minimum and maximum counting rates was larger in Obs. 2 and Obs. 3. Therefore, we suggest that the smooth ψ_X rotation behavior may accompany more pronounced spectral and flux fluctuations.

3. Multiwavelength polarization analysis

Multiwavelength campaigns for the first three observations of Mrk 421 are reported in Di Gesu et al. (2022, 2023). During Obs. 4, Mrk 421 was observed with the VLBA, the Effelsberg 100-m Radio Telescope, the Korean VLBI Network (KVN), the Submillimeter Array (SMA), the Kanata telescope, the Perkins telescope, and the Sierra Nevada Observatory (SNO, T90 telescope). Details of the observations and observatories can be found in Appendix A.3.

We have analyzed VLBA data obtained for Mrk 421 within the BEAM-ME (Blazars Entering the Astrophysical Multimessenger Era) program[1] during the period from MJD 59616 (2022 February 5) to MJD 59986 (2023 February 11) to investigate the parsec-scale jet behavior during the *IXPE* observations. The data include total and polarized intensity images at 43 GHz at 12 epochs. The data reduction and modeling are described in §A.4.

[1] www.bu.edu/blazars/BEAM-ME.html

The parsec-scale jet of Mrk 421 is strongly core-dominated, with the extended jet contributing an average of only 17% of the core flux density at 43 GHz. We consider the core to be a stationary feature of the jet and designate it as A0. During the one-year period analyzed here, we have detected two stationary features in the jet in addition to the core, A1 and A2, located at distances of ~0.4 and ~0.8 mas from A0, respectively (see Table A.3). Dominance by stationary structures is a well-documented property of the Mrk 421 jet (Lico et al. 2012; Jorstad et al. 2017; Lister et al. 2021; Weaver et al. 2022). Nonetheless, we have found motion in the jet, which we identify with a prominent polarized feature, P, which has a subluminal apparent speed β_{app}=0.7±0.1 in units of c. Figure 7 presents a sequence of images at epochs where the knot is prominent. Figure A.5 shows that knot P had a high degree of polarization, with ψ_P almost aligned with the jet direction, as expected if feature P was a transverse shock in the jet. According to its kinematics, the knot passed through the core on 2022 March 14 (MJD 59653±80, Figure A.3). If one considers the sizes of A0 and P listed in Table A.3, plus the proper motion of P (§A.4), it should have taken 107±19 days for knot P to leave the core completely, which should have occurred within 2022 June 10 – July 8. This means that during *IXPE* Obs. 1, Obs. 2, and Obs. 3, knot P was within the millimeter-wave core.

The Effelsberg 100-m Telescope observation was obtained within the framework of the QUIVER program (Monitoring the Stokes **Q**, **U**, **I** and **V** **E**mission of AGN jets in **R**adio) on 2022 December 2 (MJD 59915.11). The linear polarization was measured at 3 bands: 4.85 GHz, 8.35 GHz and 10.45 GHz. Its polarization degree was found to be 0.9±0.2%, 1.2±0.4%, and 1.2±0.2%. and its polarization angle 96.3±3.5°, 134.8±4.9°, and 159.2±7.2°, respectively. The KVN observations, with the antennas combined to act as a single dish, were performed on
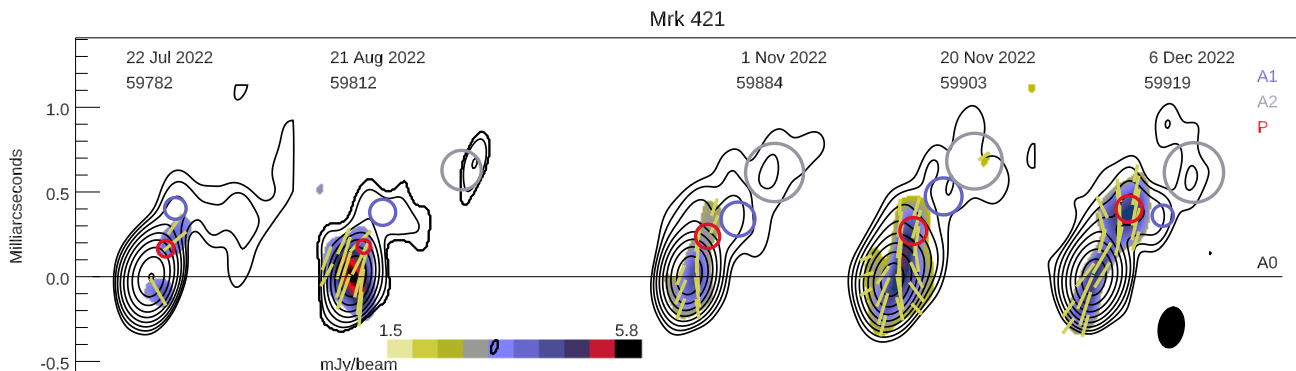
Fig. 7: VLBA total (contours) and polarized (color scale) intensity images of Mrk 421 at 43 GHz. The peak of the total intensity is 295 mJy/beam; yellow linear segments within the images indicate the direction of polarization; black horizontal line marks the position of the core, *A0*; colored circles indicate locations of jet features *A1* (blue), *A2* (gray), and *P* (red). Images are convolved with the same elliptical Gaussian beam, which is shown in the bottom right corner by a black ellipse.

2022 December 9 (MJD 59922.73) at 22, 43, 86, and 129 GHz. The linear polarization was measured as $\Pi_{22\text{GHz}}=2.4\pm0.7\%$ along $\psi_{22\text{GHz}}=30\pm12°$ at 22 GHz and $\Pi_{43\text{GHz}}=2.7\pm0.5\%$ along $\psi_{43\text{GHz}}=142\pm9°$ at 43 GHz. The measured values of Π at 86 GHz (3.1±2.3%) and 129 GHz (4.4±2.0%) are not significant detections. The polarization was measured with the SMA at 225.5 GHz as $\Pi_{225\text{GHz}}=2.0\pm0.3\%$ along position angle $\psi_{225\text{GHz}}=163\pm3°$. At the same time, the intrinsic polarization degree (after subtraction of the host-galaxy flux) in the optical R-band from SNO was $\Pi_O=4.6\pm1.3\%$ along $\psi_O=206\pm9°$. The Perkins telescope obtained optical R-band polarization covering Obs. 4 from 2022 November 26 (MJD 59909) to December 17 (MJD 59930) to give the average optical polarization parameters just before and after Obs. 4, which can be compared with the SNO measurement. In the infrared J and optical R bands, the Kanata telescope data (not corrected for the host-galaxy depolarization) yield $\Pi_J=2.41\pm0.02\%$ and $\Pi_O=2.1\pm0.03\%$ along $\psi_J=176\pm0.2°$ and $\psi_O=167.0\pm0.3°$, respectively. The latter is similar to previous Mrk 421 R-band observations with the Kanata telescope, for which an intrinsic value of $\Pi_O\approx3.3\%$ was derived (Di Gesu et al. 2023), which is consistent with the SNO measurement. All of the new multiwavelength polarimetry results conducted during Obs. 4 are summarized in Table A.2.

Figure A.2 exhibits the evolution of polarization properties of Mrk 421 obtained from the contemporaneous multiwavelength polarimetry campaign from just before *IXPE* Obs. 1 to shortly after Obs. 4. Throughout this time period, we find a similar strong chromatic behavior, with Π 2–3 times higher at X-ray rather than at longer wavelengths. In contrast, the infrared, optical, and radio degrees of polarization were similar. Meanwhile, the polarization position angle exhibited marked changes, with different values during the various *IXPE* pointings. The range of ψ observed in Obs. 1 across millimeter to X-ray wavelengths was ~30°, whereas a larger range of ~90° was evident in Obs. 4. Moreover, (Di Gesu et al. 2023) have reported that, during the rotation of ψ_X of Obs. 2 and Obs. 3, ψ values at other wavelengths were consistent with each other, with a weak temporal variation. Hence, we conclude that the region where the polarized X-rays are emitted is mostly or completely distinct from that at longer wavelengths.

Furthermore, Mrk 421 exhibited a clockwise ψ_O rotation of approximately 120° over ~40 days during the first three *IXPE*

observation periods. Similar behavior has been reported in previous optical polarimetry monitoring studies, where the polarization angle changed by ~180° over ~50 days (Blinov et al. 2015; Jermak et al. 2016; Blinov et al. 2016a; Fraija et al. 2017; Blinov et al. 2018). The direction of the ψ_O rotation was opposite to the counter-clockwise ψ_X rotation observed by *IXPE* during Obs. 2 and Obs. 3.

4. Discussion

Previous *IXPE* observations of HSPs Mrk 421 (Di Gesu et al. 2022, 2023) and Mrk 501 (Liodakis et al. 2022) suggest that an energy-stratified shock can most readily explain the ~2–3 times higher degree of polarization at X-ray rather than at longer wavelengths. In this work, we have found consistent multiwavelength measurements from Obs. 4. In this energy-stratified shock model, the relativistic electrons convert their energy to radiation as they move farther from the shock front (Marscher & Gear 1985; Tavecchio et al. 2018). The particles are efficiently accelerated at the shock front, where the magnetic field is relatively well ordered, and hence emit X-ray synchrotron radiation with relatively high polarization. Conversely, electrons lose energy as they propagate away from the shock, causing them to radiate at longer wavelengths, and the degree of polarization decreases as they encounter increasingly turbulent magnetic fields (Di Gesu et al. 2022, 2023; Liodakis et al. 2022). Hence, higher Π is predicted at higher frequencies. This effect ceases at wavelengths long enough that the electrons radiating at those wavelengths can cross the entire shocked region before losing most of their energy (Marscher & Gear 1985). This limitation can explain the similar polarization from millimeter to optical wavelengths observed in Mrk 421. It is also possible that the longer wavelength emission occurred mainly in a relatively slow sheath surrounding a much faster X-ray emitting spine of the jet (e.g., Di Gesu et al. 2023). This is consistent with the subluminal speed we have measured for knot *P*. In this case, the X-ray and longer wavelength polarization properties may not be related, consistent with their different position angles.

We therefore consider two possible geometries for an energy-stratified jet in Mrk 421: linear and radial models, as suggested by Di Gesu et al. (2022, 2023). In the case of linear geometry, the energy stratification and the ψ rotation can be explained

by emission features propagating downstream in the jet, following the helical magnetic field. On the other hand, the radial structure can correspond to a helical, rotating innermost region and a surrounding layer, similar to the spine-sheath jet model (Chhotray et al. 2017). The currently available observational data are insufficient to discern between the linear and radial geometries. Nevertheless, the episodic variation in polarization observed during Obs. 4 offers further insights into the internal geometry of the jet. For instance, it implies alternative perspectives on the geometric structure within the jet, including the intricate interactions between coexisting stable and rotating magnetic field structures, as well as stochastic transitions within the dominant magnetic field structure responsible for particle acceleration. Therefore, future observations of polarization variability are expected to yield further evidence about the geometric structure inside the jet.

On the other hand, despite the comparable multiwavelength results reported for Mrk 421 and Mrk 501, we have found a difference in the behavior of ψ_X between them. In the case of Mrk 421, ψ_{43GHz} and ψ_X exhibited significant variations without any consistent alignment with either each other or the direction of the jet axis. However, in the case of Mrk 501, an alignment was observed (within the uncertainties) between measurements of the position angle of the jet axis, ψ_X, and ψ_{43GHz} conducted within a month of each other (Liodakis et al. 2022). Further *IXPE* and VLBA observations of HSPs are needed to confirm whether, and if so, why, Mrk 421 is different in this regard.

We have found that the X-ray flux and hardness ratio of Mrk 421 were less variable during Obs. 1 and Obs. 4, when ψ_X was essentially constant, than during the ψ_X rotation of Obs. 2 and Obs. 3. This implies different physical conditions within the jet between the rotating and nonrotating states. Instead, the similar values of Π_X across all observations suggest that the basic particle acceleration scenario remained roughly independent of the magnetic field geometry. This can be accommodated within the energy-stratified shock scenario, since the degree of order of the magnetic field could be similar whether the shock moves along a straight or helical trajectory. The flux and spectral variations during the rotation event could have been caused by changes in the Doppler factor as the shock executed helical motion, although the data are too sparsely sampled to test this. Future X-ray spectroscopic and polarimetric observations with improved time resolution can potentially test whether spiral motion along a helical magnetic field causes cyclical Doppler factor variations that lead to observed variations in flux, hardness ratio, and polarization.

Our examination of a sequence of 43 GHz VLBA images has revealed the presence of a prominent, highly polarized knot moving away from the "core" at a speed of $0.7c$ during a time span that includes Obs. 1 - Obs. 3 (see Figure A.3).

This finding suggests a potential connection between the morphological changes near the jet core region and the variability in polarization, as discussed in Di Gesu et al. (2023). The knot could represent a shock containing relativistic electrons accelerated up to Lorentz factor $\sim 10^6$ that radiate at X-ray energies. However, in this scenario, it is difficult to explain the difference in the behavior of ψ_X between Obs. 1 and Obs. 2 - Obs. 3, unless the geometry of the magnetic field varies across the core, with a tighter helical structure toward the downstream end. However, our analysis does not indicate a direct connection between the X-ray polarization position angle and that of either the core or knot P (see Figure A.5), although the degree of polarization of P, 15-20%, is comparable to Π_X. This apparent lack of connection supports the conclusion, drawn above, that emission regions
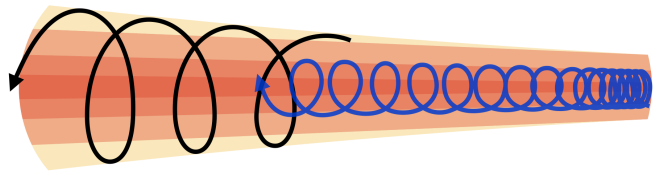

Fig. 8: Schematic diagram of double helical magnetic field components inside the jet. The downstream direction of the jet is to the left. The arrows indicate each helical magnetic field component involved in the emission at different wavelengths (blue: X-ray, black: longer wavelengths).

at longer wavelengths (millimeter, IR, and optical) were separate from, or only partially coincident with, that of the X-ray emission.

In the case of Obs. 4, there is no apparent connection between the values of ψ of the polarized features in the jet observed on 2022 December 6 (MJD 59919) and ψ_X (Fig. A.5). However, Figure A.4 indicates an increase of the core flux density in 2023 February (MJD 59986) that could be a signature of an emerging moving feature that would have been upstream of the 43 GHz VLBI core during *IXPE* Obs. 4. Further combined *IXPE* and VLBI monitoring could help to clarify whether there is any relation between the X-ray emission regions and features seen in the jet at millimeter wavelength.

We note that, from Obs. 1 to Obs. 3, the polarization angle at optical, IR, and radio wavelengths rotated in the opposite direction relative to the 5-day rotation of ψ_X during Obs. 2 and Obs. 3. This finding supports the conclusion that the X-ray emission region is separate from that at longer wavelengths. The observed similarity in radio to optical polarization properties implies that the emission at these wavelengths originates from spatially interconnected regions. The longer (relative to X-ray) rotation time scale suggests that the X-ray emission region is smaller than that of these other wavelengths. Although the polarization vector rotation at longer wavelengths could be explained by propagation of a larger emission feature down a helical magnetic field (as in Figure 8), the long-term behavior of the optical polarization of Mrk 421 implies stochastic, rather than systematic, variations of both ψ_O and Π_O (Marscher & Jorstad 2022).

5. Conclusions

We have reported X-ray, optical, IR, and radio polarization and flux measurements of the HSP blazar Mrk 421, including four *IXPE* pointings between 2022 May and December. Such observations probe the magnetic field structure and particle acceleration mechanisms inside the jets of blazars. The combined 7 months of observations sample the time and energy dependence of the X-ray polarization. Over this time span, ψ_X varied over the full range of $\sim 180°$, including a 5-day episode of rotation, while the degree of polarization maintained a value between $\sim$10–15% across all *IXPE* pointings. The X-ray flux varied by a higher fraction during the rotation than during the two *IXPE* observations without rotations.

The simultaneous multiwavelength polarimetry results over four *IXPE* observations provide evidence useful for constraining the physics of the jet. The degree of X-ray polarization was

typically ~2–3 times greater than that at longer wavelengths at all epochs sampled, while the polarization angles fluctuated. The discrepancy between the results of X-ray compared with radio, IR, and optical polarimetry supports the previous conclusion that the X-ray emission region is distinct from that at longer wavelengths in HSP blazars (Liodakis et al. 2022; Di Gesu et al. 2022, 2023). As with these previous studies, we conclude that the observations are consistent with the energy stratified shock model, with the level of turbulence increasing with distance from the shock front.

One difference between Mrk 421 and Mrk 501 is that there is no apparent correlation between the direction of the jet from VLBA and ψ_X in the former. While this could be due to the bending of the jet from the X-ray to the radio emitting region, amplified by the narrow angle to the line of sight, the optical polarization angle is also much more highly variable in Mrk 421 than in Mrk 501 (Marscher & Jorstad 2022). This implies an intrinsic difference between the two objects that should be explored with further observations.

Following Di Gesu et al. (2023), we have proposed a linear and a radial stratification scenarios to explain the rotation behavior of ψ_X. The accompanying spectral variation during the ψ_X rotation suggests that the physical conditions of the jet, such as the energy distribution of relativistic electrons, differed between the periods of rotation and nonrotation. In addition, we reported rotation in the opposite direction of the ψ between the X-ray and other wavelengths, with the latter occurring over a much longer time scale. This could potentially be interpreted by the presence of multi helical magnetic field structures inside the jet. Morphological changes in the parsec-scale jet, possibly associated with the contemporaneous emergence of a new knot of emission observed to move down the jet in 43 GHz VLBA images, may be linked to the ψ_X rotation, although differences in the radio and X-ray polarization angles argue against such a connection.

In conclusion, the present study continues to develop a new perspective on the physical and geometrical features of the magnetic field inside the jets of blazars by employing polarimetry that extends from radio to X-ray wavelengths. The *IXPE* observations, incorporating data at other wavelengths, have played a significant role in constraining the emission arising from the innermost regions of the jet. The polarization properties, sampled over different time scales and energy regimes, suggest a possible connection between spectral and polarization variations. The connection may include morphological changes in radio images, which coincided with a period of ψ_X rotation. However, due to infrequent data sampling, there remain uncertainties regarding apparent correlations, which can be chance coincidences. In addition, thus far the *IXPE* observations of Mrk 421 have been obtained when the blazar was in average activity states. It is of great interest to determine whether the polarization and physical properties change during strong flaring events. As the *IXPE* mission continues, further studies of Mrk 421 and other blazars are expected to provide the data needed to improve our understanding of the magnetic field geometry and particle acceleration processes in relativistic jets.

References

Abdo, A. A., Ackermann, M., Agudo, I., et al. 2010, ApJ, 716, 30
Agudo, I., Thum, C., Wiesemeyer, H., et al. 2012, A&A, 541, A111
Aharonian, F. A. 2000, New A, 5, 377
Akitaya, H., Moritani, Y., Ui, T., et al. 2014, in Society of Photo-Optical Instrumentation Engineers (SPIE) Conference Series, Vol. 9147, Ground-based and Airborne Instrumentation for Astronomy V, ed. S. K. Ramsay, I. S. McLean, & H. Takami, 91474O
Arnaud, K. A. 1996, in Astronomical Society of the Pacific Conference Series, Vol. 101, Astronomical Data Analysis Software and Systems V, ed. G. H. Jacoby & J. Barnes, 17
Aumont, J., Conversi, L., Thum, C., et al. 2010, A&A, 514, A70
Baldini, L., Barbanera, M., Bellazzini, R., et al. 2021, Astroparticle Physics, 133, 102628
Baldini, L., Buccantini, N., Lalla, N. D., et al. 2022, SoftwareX, 19, 101194
Baloković, M., Paneque, D., Madejski, G., et al. 2016, ApJ, 819, 156
Bellazzini, R., Angelini, F., Baldini, L., et al. 2003, in Society of Photo-Optical Instrumentation Engineers (SPIE) Conference Series, Vol. 4843, Polarimetry in Astronomy, ed. S. Fineschi, 372–382
Bellazzini, R., Spandre, G., Minuti, M., et al. 2007, Nuclear Instruments and Methods in Physics Research A, 579, 853
Blinov, D., Pavlidou, V., Papadakis, I., et al. 2018, MNRAS, 474, 1296
Blinov, D., Pavlidou, V., Papadakis, I., et al. 2016a, MNRAS, 462, 1775
Blinov, D., Pavlidou, V., Papadakis, I., et al. 2015, MNRAS, 453, 1669
Blinov, D., Pavlidou, V., Papadakis, I. E., et al. 2016b, MNRAS, 457, 2252
Böttcher, M. 2019, Galaxies, 7, 20
Böttcher, M., Reimer, A., Sweeney, K., & Prakash, A. 2013, ApJ, 768, 54
Chhotray, A., Nappo, F., Ghisellini, G., et al. 2017, MNRAS, 466, 3544
Costa, E., Soffitta, P., Bellazzini, R., et al. 2001, Nature, 411, 662
Dermer, C. D. & Schlickeiser, R. 1993, ApJ, 416, 458
Di Gesu, L., Donnarumma, I., Tavecchio, F., et al. 2022, ApJ, 938, L7
Di Gesu, L., Marshall, H. L., Ehlert, S. R., et al. 2023, Nature Astronomy
Di Marco, A., Costa, E., Muleri, F., et al. 2022, AJ, 163, 170
Di Marco, A., Soffitta, P., Costa, E., et al. 2023, AJ, 165, 143
Donnarumma, I., Vittorini, V., Vercellone, S., et al. 2009, ApJ, 691, L13
Ehlert, S. R., Ferrazzoli, R., Marinucci, A., et al. 2022, ApJ, 935, 116
Fabiani, S., Costa, E., Bellazzini, R., et al. 2012, Advances in Space Research, 49, 143
Fabiani, S. & Muleri, F. 2014, Astronomical X-Ray Polarimetry, Astronomia e astrofisica (Aracne)
Fossati, G., Maraschi, L., Celotti, A., Comastri, A., & Ghisellini, G. 1998, MNRAS, 299, 433
Fraija, N., Benítez, E., Hiriart, D., et al. 2017, ApJS, 232, 7
Gianolli, V. E., Kim, D. E., Bianchi, S., et al. 2023, MNRAS, 523, 4468
HI4PI Collaboration, Ben Bekhti, N., Flöer, L., et al. 2016, A&A, 594, A116
Ho, P. T. P., Moran, J. M., & Lo, K. Y. 2004, ApJ, 616, L1
Hovatta, T. & Lindfors, E. 2019, New A Rev., 87, 101541
Hovatta, T., Lindfors, E., Blinov, D., et al. 2016, A&A, 596, A78
Jermak, H., Steele, I. A., Lindfors, E., et al. 2016, MNRAS, 462, 4267
Jones, T. W., O'Dell, S. L., & Stein, W. A. 1974, ApJ, 188, 353
Jorstad, S. G., Marscher, A. P., Morozova, D. A., & et al. 2017, ApJ, 846, id 98
Kang, S., Lee, S.-S., & Byun, D.-Y. 2015, Journal of Korean Astronomical Society, 48, 257
Kawabata, K. S., Okazaki, A., Akitaya, H., et al. 1999, PASP, 111, 898
Kislat, F., Clark, B., Beilicke, M., & Krawczynski, H. 2015, Astroparticle Physics, 68, 45
Kraus, A., Krichbaum, T. P., Wegner, R., et al. 2003, A&A, 401, 161
Lico, R., Giroletti, M., Orienti, M., & et al. 2012, A&A, 545, id A117
Liodakis, I., Marscher, A. P., Agudo, I., et al. 2022, Nature, 611, 677
Liodakis, I., Peirson, A. L., & Romani, R. W. 2019, ApJ, 880, 29
Lister, M. L., Homan, D. C., Kellermann, K. I., & et al. 2021, ApJ, 923, id 30
Mannheim, K. 1993, A&A, 269, 67
Maraschi, L., Ghisellini, G., & Celotti, A. 1992, ApJ, 397, L5
Marrone, D. P. & Rao, R. 2008, in Society of Photo-Optical Instrumentation Engineers (SPIE) Conference Series, Vol. 7020, Millimeter and Submillimeter Detectors and Instrumentation for Astronomy IV, ed. W. D. Duncan, W. S. Holland, S. Withington, & J. Zmuidzinas, 70202B
Marscher, A. P. & Gear, W. K. 1985, ApJ, 298, 114
Marscher, A. P. & Jorstad, S. G. 2022, Universe, 8, 644
Marscher, A. P., Jorstad, S. G., D'Arcangelo, F. D., et al. 2008, Nature, 452, 966
Marscher, A. P., Jorstad, S. G., & Larionov, V. M., et al. 2010, ApJ, 710, L126
Marshall, H. L. 2021a, AJ, 162, 134
Marshall, H. L. 2021b, ApJ, 907, 82
Massaro, E., Perri, M., Giommi, P., & Nesci, R. 2004, A&A, 413, 489
Middei, R., Giommi, P., Perri, M., et al. 2022, MNRAS, 514, 3179
Middei, R., Perri, M., Puccetti, S., et al. 2023, ApJ, 953, L28
Muleri, F. 2022, arXiv e-prints, arXiv:2204.12739
Myserlis, I., Angelakis, E., Kraus, A., et al. 2018, A&A, 609, A68
Nilsson, K., Pasanen, M., Takalo, L. O., et al. 2007, A&A, 475, 199

Piconcelli, E., Jimenez-Bailón, E., Guainazzi, M., et al. 2004, MNRAS, 351, 161
Primiani, R. A., Young, K. H., Young, A., et al. 2016, Journal of Astronomical Instrumentation, 5, 1641006
Rankin, J., Muleri, F., Tennant, A. F., et al. 2022, The Astronomical Journal, 163, 163
Rybicki, G. B. & Lightman, A. P. 1979, Radiative processes in astrophysics
Sikora, M., Begelman, M. C., & Rees, M. J. 1994, ApJ, 421, 153
Strohmayer, T. E. 2017, ApJ, 838, 72
Tavecchio, F. 2021, Galaxies, 9, 37
Tavecchio, F., Landoni, M., Sironi, L., & Coppi, P. 2018, MNRAS, 480, 2872
Weaver, Z. R., Jorstad, S. G., Marscher, A. P., et al. 2022, ApJS, 260, 12
Weisskopf, M. C., Soffitta, P., Baldini, L., et al. 2022, Journal of Astronomical Telescopes, Instruments, and Systems, 8, 026002
Wilms, J., Allen, A., & McCray, R. 2000, ApJ, 542, 914
Zhang, H. 2019, Galaxies, 7, 85

[1] INAF Istituto di Astrofisica e Planetologia Spaziali, Via del Fosso del Cavaliere 100, 00133 Roma, Italy
[2] Dipartimento di Fisica, Università degli Studi di Roma "La Sapienza", Piazzale Aldo Moro 5, 00185 Roma, Italy
[3] Dipartimento di Fisica, Università degli Studi di Roma "Tor Vergata", Via della Ricerca Scientifica 1, 00133 Roma, Italy
[4] ASI - Agenzia Spaziale Italiana, Via del Politecnico snc, 00133 Roma, Italy
[5] Finnish Centre for Astronomy with ESO, 20014 University of Turku, Finland
[6] Institute for Astrophysical Research, Boston University, 725 Commonwealth Avenue, Boston, MA 02215, USA
[7] Saint Petersburg State University, 7/9 Universitetskaya nab., St. Petersburg, 199034 Russia
[8] Space Science Data Center, Agenzia Spaziale Italiana, Via del Politecnico snc, 00133 Roma, Italy
[9] INAF Osservatorio Astronomico di Roma, Via Frascati 33, 00078 Monte Porzio Catone (RM), Italy
[10] MIT Kavli Institute for Astrophysics and Space Research, Massachusetts Institute of Technology, 77 Massachusetts Avenue, Cambridge, MA 02139, USA
[11] Instituto de Astrofísica de Andalucía—CSIC, Glorieta de la Astronomía s/n, 18008 Granada, Spain
[12] INAF Osservatorio Astronomico di Brera, Via E. Bianchi 46, 23807 Merate (LC), Italy
[13] Dipartimento di Fisica, Università degli Studi di Torino, Via Pietro Giuria 1, 10125 Torino, Italy
[14] Istituto Nazionale di Fisica Nucleare, Sezione di Torino, Via Pietro Giuria 1, 10125 Torino, Italy
[15] University of Maryland, Baltimore County, Baltimore, MD 21250, USA
[16] NASA Goddard Space Flight Center, Greenbelt, MD 20771, USA
[17] Louisiana State University, Baton Rouge, LA 70803, USA
[18] Istituto Nazionale di Fisica Nucleare, Sezione di Roma "Tor Vergata", Via della Ricerca Scientifica 1, 00133 Roma, Italy
[19] Department of Astronomy, University of Maryland, College Park, Maryland 20742, USA
[20] Hiroshima Astrophysical Science Center, Hiroshima University, 1-3-1 Kagamiyama, Higashi-Hiroshima, Hiroshima 739-8526, Japan
[21] Department of Physics, Graduate School of Advanced Science and Engineering, Hiroshima University Kagamiyama, 1-3-1 Higashi-Hiroshima, Hiroshima 739-8526, Japan
[22] Core Research for Energetic Universe (Core-U), Hiroshima University, 1-3-1 Kagamiyama, Higashi-Hiroshima, Hiroshima 739-8526, Japan
[23] Department of Physics, Tokyo Institute of Technology, 2-12-1 Ookayama, Meguro-ku, Tokyo 152-8551, Japan
[24] Planetary Exploration Research Center, Chiba Institute of Technology 2-17-1 Tsudanuma, Narashino, Chiba 275-0016, Japan
[25] Institut de Radioastronomie Millimétrique, Avenida Divina Pastora 7, Local 20, E-18012 Granada, Spain
[26] Max-Planck-Institut für Radioastronomie, Auf dem Hügel 69, D-53121 Bonn, Germany

[27] Section of Astrophysics, Astronomy & Mechanics, Department of Physics, National and Kapodistrian University of Athens, Panepistimiopolis Zografos 15784, Greece

[28] Korea Astronomy and Space Science Institute, Daedeokdae-ro 776, Yuseong-gu, Daejeon 34055, Republic of Korea

[29] University of Science and Technology, Gajeong-ro 217, Yuseong-gu, Daejeon 34113, Republic of Korea

[30] Center for Astrophysics | Harvard & Smithsonian, 60 Garden St, Cambridge, MA 02138, USA

[31] Department of Physics and Astronomy, 20014 University of Turku, Finland

[32] Department of Physics, University of Crete, 70013, Heraklion, Greece

[33] Institute of Astrophysics, Foundation for Research and Technology-Hellas, GR-71110 Heraklion, Greece

[34] Owens Valley Radio Observatory, California Institute of Technology, MC 249-17, Pasadena, CA 91125, USA

[35] Special Astrophysical Observatory, Russian Academy of Sciences, 369167, Nizhnii Arkhyz, Russia

[36] Pulkovo Observatory, St.Petersburg, 196140, Russia

[37] INAF Osservatorio Astronomico di Cagliari, Via della Scienza 5, 09047 Selargius (CA), Italy

[38] Istituto Nazionale di Fisica Nucleare, Sezione di Pisa, Largo B. Pontecorvo 3, 56127 Pisa, Italy

[39] Dipartimento di Fisica, Università di Pisa, Largo B. Pontecorvo 3, 56127 Pisa, Italy

[40] NASA Marshall Space Flight Center, Huntsville, AL 35812, USA

[41] Dipartimento di Matematica e Fisica, Università degli Studi Roma Tre, Via della Vasca Navale 84, 00146 Roma, Italy

[42] INAF Osservatorio Astrofisico di Arcetri, Largo Enrico Fermi 5, 50125 Firenze, Italy

[43] Dipartimento di Fisica e Astronomia, Università degli Studi di Firenze, Via Sansone 1, 50019 Sesto Fiorentino (FI), Italy

[44] Istituto Nazionale di Fisica Nucleare, Sezione di Firenze, Via Sansone 1, 50019 Sesto Fiorentino (FI), Italy

[45] Science and Technology Institute, Universities Space Research Association, Huntsville, AL 35805, USA

[46] Department of Physics and Kavli Institute for Particle Astrophysics and Cosmology, Stanford University, Stanford, California 94305, USA

[47] Institut für Astronomie und Astrophysik, Universität Tübingen, Sand 1, 72076 Tübingen, Germany

[48] Astronomical Institute of the Czech Academy of Sciences, Boční II 1401/1, 14100 Praha 4, Czech Republic

[49] RIKEN Cluster for Pioneering Research, 2-1 Hirosawa, Wako, Saitama 351-0198, Japan

[50] California Institute of Technology, Pasadena, CA 91125, USA

[51] Yamagata University,1-4-12 Kojirakawa-machi, Yamagata-shi 990-8560, Japan

[52] Osaka University, 1-1 Yamadaoka, Suita, Osaka 565-0871, Japan

[53] University of British Columbia, Vancouver, BC V6T 1Z4, Canada

[54] Department of Physics, Faculty of Science and Engineering, Chuo University, 1-13-27 Kasuga, Bunkyo-ku, Tokyo 112-8551, Japan

[55] Department of Physics and Astronomy and Space Science Center, University of New Hampshire, Durham, NH 03824, USA

[56] Physics Department and McDonnell Center for the Space Sciences, Washington University in St. Louis, St. Louis, MO 63130, USA

[57] Université de Strasbourg, CNRS, Observatoire Astronomique de Strasbourg, UMR 7550, 67000 Strasbourg, France

[58] Graduate School of Science, Division of Particle and Astrophysical Science, Nagoya University, Furo-cho, Chikusa-ku, Nagoya, Aichi 464-8602, Japan

[59] Department of Physics, The University of Hong Kong, Pokfulam, Hong Kong

[60] Department of Astronomy and Astrophysics, Pennsylvania State University, University Park, PA 16802, USA

[61] Université Grenoble Alpes, CNRS, IPAG, 38000 Grenoble, France

[62] Dipartimento di Fisica e Astronomia, Università degli Studi di Padova, Via Marzolo 8, 35131 Padova, Italy

[63] Mullard Space Science Laboratory, University College London, Holmbury St Mary, Dorking, Surrey RH5 6NT, UK

[64] Anton Pannekoek Institute for Astronomy & GRAPPA, University of Amsterdam, Science Park 904, 1098 XH Amsterdam, The Netherlands

[65] Guangxi Key Laboratory for Relativistic Astrophysics, School of Physical Science and Technology, Guangxi University, Nanning 530004, China

Appendix A: Observation and data reduction

A.1. IXPE data

We obtained cleaned level 2 *IXPE* data processed by a standard *IXPE* pipeline from the Science Operation Center (SOC)[2]. The pipeline includes the photoelectron events correction in the Gas Pixel Detector (GPD, Costa et al. 2001; Bellazzini et al. 2007; Fabiani et al. 2012; Baldini et al. 2021), as well as the photoelectron track reconstruction process based on standard moments analysis (Bellazzini et al. 2003; Fabiani & Muleri 2014; Di Marco et al. 2022). In particular, the pipeline rectifies the fluctuations in gain properties affected by gas conditions (e.g., temperature and pressure), nonuniform charging of the Gas Electron Multiplier (GEM) material, and polarization artifacts induced by spurious modulation (Rankin et al. 2022). The level 2 data of *IXPE* contain the time of arrival, position, and energy of each photon event, along with polarization information represented by the Q and U Stokes parameters.

The scientific data analysis was performed using the public `ixpeobssim` software version 30.2.1 (Baldini et al. 2022). First, we extracted the source and background data using an optimized region selection criterion as suggested by Di Marco et al. (2023). The source data were extracted from a circular region with a 60″ radius, while the background data were extracted from an annular source-free region with inner and outer radii of 150″ and 300″, respectively. Both regions were centered on the source position in the detector frame. Next, we created the polarization cube (PCUBE) and the Stokes parameter spectra (I, Q, and U) using `xpbin`. To eliminate the influence due to the background, we applied the background subtraction technique (Baldini et al. 2022) and created PCUBEs of the source and background for each detector unit. The final source polarization properties were recalibrated by considering the `BACKSCALE` ratio between the source and background ($\sim$ 0.05). In a similar way, we produced three Stokes parameter spectra for three detectors, totaling 9 spectra, using the `PHA1`, `PHAQ`, and `PHAU` algorithms in `xpbin`. We grouped the I spectra with a minimum of 30 counts in each energy bin, as required for the χ^2 statistics in the fits, and applied constant energy binning for the Q and U spectra for every 0.2 keV interval. We employed the recent version of the *IXPE* calibration database files (CALDB 20221020) contained in both `ixpeobssim` and the HEASOFT package (v6.31.1) for both the PCUBE and the Stokes parameter spectra. In particular, we utilized the weighted analysis method (Di Marco et al. 2022) on the I, Q, and U spectra to improve the significance of our measurements with `alpha075` response matrices. The flux variability was analyzed using a light curve created with the `LC` algorithms in `xpbin` of `ixpeobssim`.

The polarization error contour (Figure 1) was drawn from calibrated normalized $Q (= Q/I)$ and $\mathcal{U} (= U/I)$ at specific confidence levels (68.27%, 90.00%, and 99.0%) according to:

$$Q_{C.L.} = Q_0 + \epsilon \cos(\zeta),$$
$$\mathcal{U}_{C.L.} = \mathcal{U}_0 + \epsilon \sin(\zeta), \qquad (A.1)$$

where Q_0 and $\mathcal{U}_0$ represent the averaged Stokes parameter values, and $Q_{C.L.}$ and $\mathcal{U}_{C.L.}$ denote the Q and $\mathcal{U}$ values of a given confidence level calculated with two degrees of freedom, respectively. We note that, since we are considering two dependent variables, Π and ψ, at the same time, the error should be recalculated based on the χ^2 distribution with 2 degrees of freedom
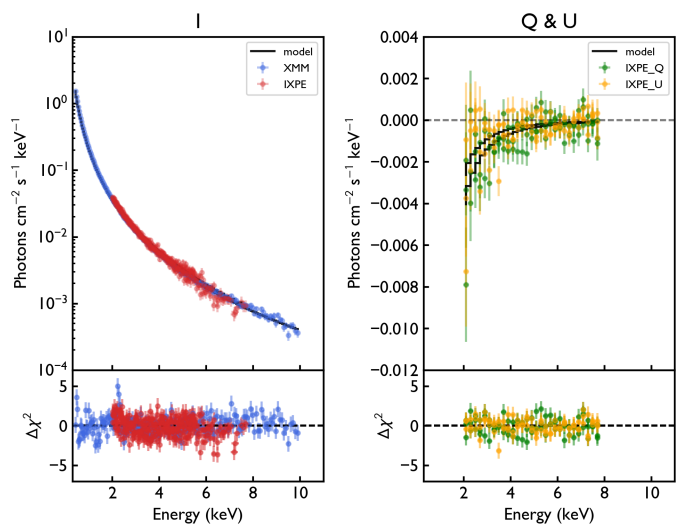

Fig. A.1: Spectropolarimetric fit of *XMM-Newton* (blue) and *IXPE I* (red), Q (green), and U (orange) spectra, with residuals of the best-fit model. The left panel displays the I spectrum with a log-parabolic model (Massaro et al. 2004), while the right panel presents the constant polarization model fit with the `POLCONST` model for Q and U spectra. The black line in both panels indicates the model fit result.

($\epsilon = \sigma \sqrt{\chi^2_{\mathrm{2\,d.o.f.}}}$, $\sigma = \sigma_Q = \sigma_\mathcal{U}$). The variable ζ follows the angle distribution from 0 to 2π.

A.2. Spectroscopic X-ray data

During *IXPE* Obs. 4, a snapshot of about 5 ks was performed with *XMM-Newton* in timing mode to limit photon pile-up. To extract the science products, we used the *XMM-Newton* Science Analysis Software (SAS), version 21, with the most updated CCF (current calibration files). Two boxed regions were adopted to extract the source spectra and background. In particular, we chose the source box to have a width of 27 pixels, as this size was found to maximize the signal-to-noise ratio. (Details of this procedure can be found in Piconcelli et al. 2004.) Then, the resulting spectrum was binned to achieve at least 30 counts in each energy bin. To allow simultaneous spectropolarimetric fitting within XSPEC, the keyword "XFLT0001 Stokes:0" was added to the headers of the corresponding PHA files.

The *Swift-XRT* monitoring consisted of ~1 ks long observations performed in Windowed Timing (WT) mode. Raw data were reduced using the standard commands within the *XRT* Data Analysis Software (XRTDAS, v. 3.6.1) and adopting the latest calibration files available in the *Swift-XRT* CALDB (version 20210915). The cleaned event files were used to extract the source spectrum from a circular region with a radius of 47″, while the background was extracted using a blank sky WT observation available in the Swift archive, also within a circular region of radius 47″. The resulting spectra were subsequently binned, requiring at least 25 counts in each energy bin.

A.3. Radio, Infrared and optical data

During all of the IXPE pointings, we observed Mrk 421 at millimeter (radio), infrared (IR), and optical wavelengths, measuring both flux density and linear polarization. The observations and data analysis for the first three observations can be found

Table A.1: Best-fit parameters from our simultaneous spectropolarimetric analysis.

MODEL = CONSTANT × TBABS × LOGPAR × POLCONST			
Component	Parameter	Units	Value (±1σ)
LOGPAR	α		2.82 ±0.005
	β		0.20 ±0.004
	pivot E	keV	5. (f)
	Norm		2.96e-3 ±1.e-5
POLCONST	Π_X	(%)	14 ±1
	ψ_X	(°)	107 ±3
TBABS	N_H	10^{22}cm^{-2}	1.34e-2 (f)
CONSTANT	*XMM-Newton*		1. (f)
	IXPE DU 1		1.11 ± 0.005
	IXPE DU 2		1.06 ± 0.005
	IXPE DU 3		1.01 ± 0.005
			χ^2 / d.o.f.= 740/650

Notes. Errors are 1σ confidence and (f) denotes a fixed parameter.

in detail in Di Gesu et al. (2022, 2023); here we provide only a short description. For Obs. 4, radio, IR, and optical observations were provided by QUIVER at the Effelsberg telescope, KVN, SMA (Ho et al. 2004), Hiroshima Optical and Near-InfraRed camera (HONIR, Akitaya et al. 2014) at the Kanata telescope, the Perkins telescope, and T90 at the Sierra Nevada Observatory (SNO).

The QUIVER observations were performed at several radio bands (depending on receiver availability and weather conditions) from 2.6 GHz to 44 GHz (11 cm to 7 mm wavelength) using six receivers located at the secondary focus of the 100-m Effelsberg Radio Telescope (S110mm, S45mm, S28mm, S20mm, S14mm, and S7mm). The receivers are equipped with two orthogonally polarized feeds (either circular or linear) that can deliver polarimetric parameters using either conventional polarimeters or by connecting the SpecPol spectropolarimetric backend. Instrumental polarization is calibrated via observations of both polarized and unpolarized calibrators performed in each session, and then removed from the data (e.g., Myserlis et al. 2018; Kraus et al. 2003). The polarized intensity, degree, and position angle were derived from the Stokes I, Q, and U cross-scans. The total flux density was successfully recovered at 13 bands between 4.85 GHz and 43.75 GHz. The calibrators 3C 286, 3C 48, and NGC 7027 were used for the total flux and polarization calibration (e.g., Myserlis et al. 2018; Kraus et al. 2003).

Observations were conducted with the KVN simultaneously at 4 frequencies from 22 to 129 GHz in single-dish mode. This was achieved by using the Tamna (22, 43 GHz) and Yonsei (86,129 GHz) antennas with circularly polarized feed horns to conduct two-frequency dual-polarization observations. The polarization angle was calibrated using the Crab nebula (152°; Aumont et al. 2010), and the polarization degree using Jupiter (unpolarized) and 3C286 (polarized, Agudo et al. 2012) following Kang et al. (2015).

The SMA observations were taken at 225.538 GHz (1.3 mm) through the SMAPOL program (SMA Monitoring of AGN with POLarization). The SMAPOL observations were taken on 2022 December 7 (MJD 59920) in full polarization mode (Marrone &

Rao 2008) using the SWARM correlator (Primiani et al. 2016), and calibrated with the MIR software package [3].

Observations using HONIR were taken on 2022 December 6 (MJD 59919.7537) in the R and J bands[4]. Each observation comprised four exposures in different positions of the half-wave plate (Kawabata et al. 1999), which were then used to estimate the Stokes parameters and calculate the polarization degree and angle. The host galaxy of Mrk 421 contributes a significant fraction of unpolarized flux to the total emission, thereby reducing the polarization. None of the polarization degree estimates from Kanata have been corrected for the host-galaxy contribution due to the lack of the photometry data needed for such a correction, and hence they should be considered as lower limits to the intrinsic polarization degree of the blazar component.

The optical photometric and polarimetric observations were also obtained at the 1.8 m Perkins telescope (Flagstaff, AZ, USA) with the PRISM camera[5] in R band performed before and after Obs. 4. The camera includes a polarimeter with a rotating half-wave plate. Each polarization observation has consisted of four consecutive exposures of 60 s at instrumental position angles 0°, 90°, 45°, and 135° of the waveplate to calculate the normalized Stokes parameters Q and U.

The SNO observations were performed using polarized filters oriented to represent different positions of a half-wave plate, similar to a conventional polarimeter. The data are then analyzed following standard photometric procedures. Mrk 421 was observed on 2022 December 7 in the R band. In this case, following Nilsson et al. (2007) and Hovatta et al. (2016), we have corrected the host-galaxy contribution. Several observations were taken within the same night. We report the weighted average and uncertainty after considering all of the intra-night observations to account for variations of the system and the observing conditions during the rotation of the filter wheel.

A.4. VLBA observations and analysis

The VLBA data were reduced with the Astronomical Image Process System (AIPS) and *Difmap* software packages in the manner described by Jorstad et al. (2017). The total intensity images are modeled by a number of components with circular Gaussian brightness distributions, with the minimum number of components determined by the best fit between the data and model at each epoch according to a χ^2 test. We identify the brightest feature located at the southeastern end of the jet as the "core," designated as $A0$, which we assume to be a stationary feature. To obtain polarized intensity images, the data were corrected for the instrumental-polarization "D-terms," calculated by averaging the D-terms obtained individually from a number of sources (usually 15) observed along with Mrk 421 in the BEAM-ME program. The electric-vector position angle (ψ_{43GHz}) calibration was obtained by different methods, as discussed in Jorstad et al. (2017). The modeling of total intensity images provides the following parameters of each component: flux density, S, distance from the core, R, position angle with respect to the core, Θ, and angular size of the component, a (FWHM of the best-fit Gaussian). For polarized features in the jet, we have calculated the degree of polarization, Π_{knot}, and ψ_{knot}, by integrating the Q, and U Stokes parameter models obtained with *Difmap* during imaging within the size of the corresponding feature from the total

---

[3] https://lweb.cfa.harvard.edu/~cqi/mircook.html
[4] http://hasc.hiroshima-u.ac.jp/instruments/honir/filters-e.html
[5] https://www.bu.edu/prism/

Table A.2: Multiwavelength polarization properties of Mrk 421

Telescope	Band (GHz)	Dates (YYYY-MM-DD)	Radio Polarization $\Pi_R(\%)$	ψ_R (°)	Radio Flux Density (10^{-25}erg s^{-1} cm^{-2} Hz^{-1})
KVN	22	2022-12-09	2.4 ± 0.7	210 ± 12	45 ± 4
KVN	43	2022-12-09	2.7 ± 0.5	142 ± 9	40 ± 2
KVN	86	2022-12-09	3.1 ± 2.3	153 ± 15	34 ± 7
KVN	129	2022-12-09	4.4 ± 2.0	191 ± 16	71 ± 19
SMA	230	2022-12-07	2.0 ± 0.3	163 ± 3	20 ± 2
Effelsberg	4.85	2022-12-02	0.9 ± 0.2	96 ± 4	59.4 ± 1.0
Effelsberg	8.35	2022-12-02	1.2 ± 0.4	135 ± 5	50.1 ± 0.5
Effelsberg	10.45	2022-12-02	1.2 ± 0.2	159 ± 7	48.7 ± 1.1
VLBA	43	2022-12-06	1.7 ± 0.6	171 ± 10	25.9 ± 3.3
VLBA	43	2022-11-20	2.1 ± 0.4	178 ± 7	22.9 ± 3.3
VLBA	43	2022-11-01	1.5 ± 0.3	181 ± 8	27.5 ± 3.5
VLBA	43	2022-08-21	2.0 ± 0.6	166 ± 9	29.4 ± 3.6
VLBA	43	2022-07-22	1.3 ± 0.5	215 ± 13	28.8 ± 3.6
VLBA	43	2022-07-15	< 1.1	Undetermined	29.0 ± 4.1

Telescope	Band (μm)	Dates (YYYY-MM-DD)	Infrared Polarization $\Pi_{IR}(\%)$	ψ_{IR} (°)	Infrared flux density (10^{-25}erg s^{-1} cm^{-2} Hz^{-1})
Kanata [1]	J:1.1	2022-12-07	2.1 ± 0.03	167.0 ± 0.3	1.65 ± 0.03

Telescope	Band (nm)	Dates (YYYY-MM-DD)	Optical Polarization $\Pi_O(\%)$	ψ_O (°)	Optical flux density (10^{-25}erg s^{-1} cm^{-2} Hz^{-1})
SNO	R:653	2022-12-07	4.6 ± 1.3	206 ± 9	2.11 ± 0.03
Kanata [1]	R:653	2022-12-07	2.41 ± 0.02	176 ± 0.2	–
Perkins	R:653	2022-12-17	2.65 ± 0.21	151.9 ± 2.0	2.75 ± 0.03
Perkins	R:653	2022-12-17	2.68 ± 0.21	156.2 ± 2.3	2.74 ± 0.03
Perkins	R:653	2022-12-17	2.51 ± 0.21	155.9 ± 2.5	2.75 ± 0.03
Perkins	R:653	2022-12-16	1.12 ± 0.27	156.2 ± 7.2	2.87 ± 0.03
Perkins	R:653	2022-12-15	1.48 ± 0.28	160.6 ± 5.7	2.77 ± 0.03
Perkins	R:653	2022-12-14	1.74 ± 0.30	125.1 ± 5.3	2.72 ± 0.02
Perkins	R:653	2022-12-01	6.89 ± 0.39	161.7 ± 1.8	2.98 ± 0.04
Perkins	R:653	2022-12-01	7.11 ± 0.37	164.5 ± 1.7	2.99 ± 0.03
Perkins	R:653	2022-12-01	6.91 ± 0.37	159.0 ± 1.6	3.00 ± 0.03
Perkins	R:653	2022-11-28	4.76 ± 0.25	179.1 ± 1.6	2.99 ± 0.03
Perkins	R:653	2022-11-28	4.39 ± 0.28	164.4 ± 1.9	3.00 ± 0.04
Perkins	R:653	2022-11-28	5.22 ± 0.22	164.7 ± 1.3	3.00 ± 0.03
Perkins	R:653	2022-11-28	4.22 ± 0.22	168.6 ± 1.6	2.99 ± 0.03
Perkins	R:653	2022-11-27	5.79 ± 0.26	162.3 ± 1.3	2.98 ± 0.03
Perkins	R:653	2022-11-27	5.79 ± 0.21	165.3 ± 0.8	2.99 ± 0.02
Perkins	R:653	2022-11-27	5.02 ± 0.21	163.7 ± 0.8	2.98 ± 0.02
Perkins	R:653	2022-11-27	5.29 ± 0.21	163.3 ± 0.4	2.99 ± 0.02
Perkins	R:653	2022-11-26	6.42 ± 0.21	151.5 ± 0.8	2.86 ± 0.02
Perkins	R:653	2022-11-26	5.71 ± 0.23	152.0 ± 1.1	2.87 ± 0.02
Perkins	R:653	2022-11-26	5.44 ± 0.21	155.0 ± 0.9	2.86 ± 0.02

Notes. [1]Not corrected for dilution of polarization by unpolarized starlight from the host galaxy.

flux density modeling. As a result of modeling, we have detected three stationary features, $A0$, $A1$, and $A2$, and one moving knot, P in the jet of Mrk 421 during 12 epochs from 2022 February 5 to 2023 February 11. Table A.3 gives the average (over epochs) parameters of the jet features, while Figure A.3 plots the distance of all knots detected in the jet versus time, and Figure A.4 presents the light curve of the core, $A0$.

We have approximated the motion of knot P with a ballistic trajectory with proper motion μ=0.34±0.06 mas yr^{-1}, corresponding to a subluminal apparent speed (in units of c) β_{app} =

0.7 ± 0.1. The MOJAVE survey [6] at 15 GHz finds an historical maximum β_{app} ∼ 0.2 in the Mrk 421 jet. At 43 GHz, with 3 times higher angular resolution, Weaver et al. (2022) reported three knots with β_{app} > 1, with the fastest having an apparent speed of 2.41 ± 0.14 c, based on monitoring within the VLBA-BU-BLAZAR program. We have extrapolated the motion of P back to the core (as shown in Figure A.3 by a red solid line), which yields the time of ejection of P from the core [7] as MJD 59653±80 (2022 March 14). Figure A.4 plots the light curve of

---

[6] www.cv.nrao.edu/MOJAVE/sourcepages/1101+384.shtml

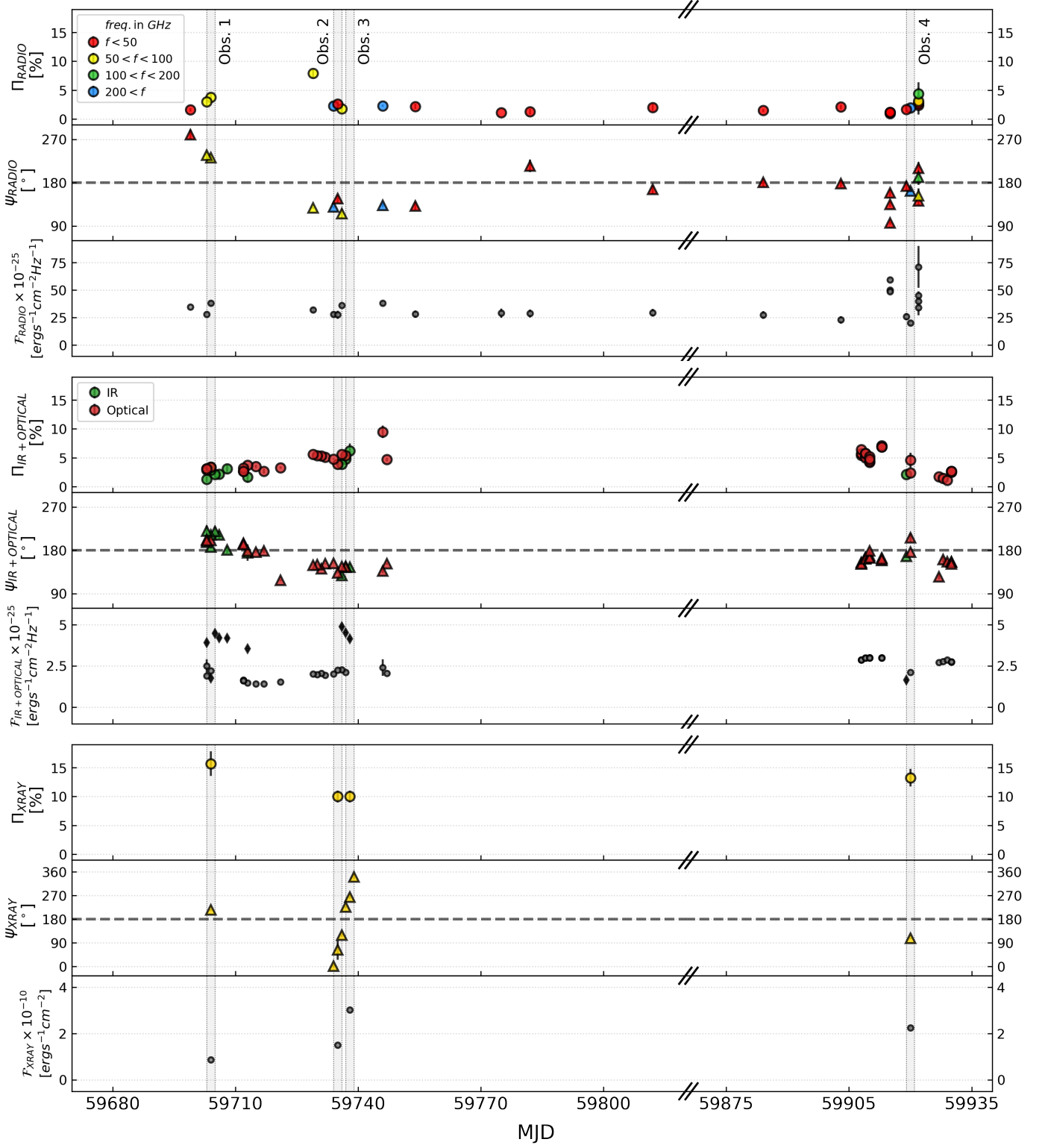[7] The time of passage of the centroid of P through the centroid of $A0$

Fig. A.2: Multiwavelength polarization versus time of Mrk 421. Each row presents the polarization degree (circle) and polarization angle (triangle), with 1σ errors measured by radio (red: $f<50$ GHz, yellow: $50<f<100$ GHz, green: $100<f<200$ GHz, blue: $f<200$ GHz), infrared (green), and optical (red), and X-ray (orange) facilities, from top to bottom. The gray shaded areas denote the durations of the four *IXPE* observations.

the core (*A0*), which has a local maximum on MJD 59699 (2022, April 30), the epoch of VLBA observation closest to the ejection time of *P*; this supports the derived time of ejection. Knot *P* possesses the highest degree of polarization in the jet, with Π_P

reaching ~20%. Another polarized feature in the jet is the core *A0*, with an average $\Pi_{A0} \sim 2\%$. Figure A.5 shows the evolution of the polarization parameters Π_{A0}, ψ_{A0}, and Π_P, ψ_P. Figures A.3 and A.5 also indicate the times of the four *IXPE* observations by

Table A.3: Average parameters of the main features in the jet of Mrk 421 at 43 GHz

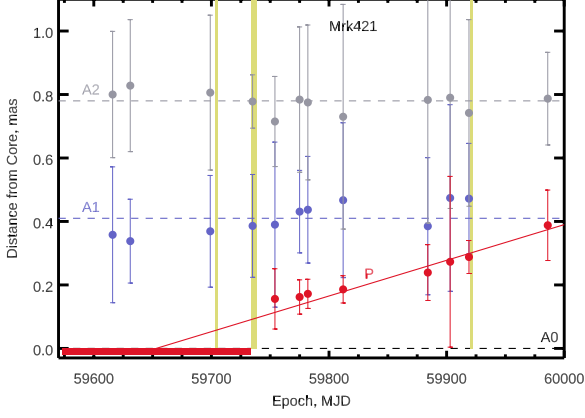| Parameter	A0	A1	A2	P
Number of epochs	12	11	12	8
Average flux, S, (Jy)	0.31 ± 0.03	0.023 ± 0.014	0.017 ± 0.008	0.014 ± 0.010
Average distance, R (mas)	–	0.41 ± 0.05	0.78 ± 0.03	0.23 ± 0.08
Average PA, Θ, (°)	–	-31 ± 10	-45 ± 5	-10 ± 12
Average Size, a, (mas)	0.06 ± 0.02	0.24 ± 0.07	0.46 ± 0.12	0.14 ± 0.07

Fig. A.3: Distance from the core of jet components $A1$ (blue circles), $A2$ (gray circles), and P (red circles) vs. time; black dotted line indicates position of the core, $A0$; the red line approximates the motion of knot P with the uncertainty of its ejection time shown by the red area on the bottom left; yellow areas mark epochs of *IXPE* observations.
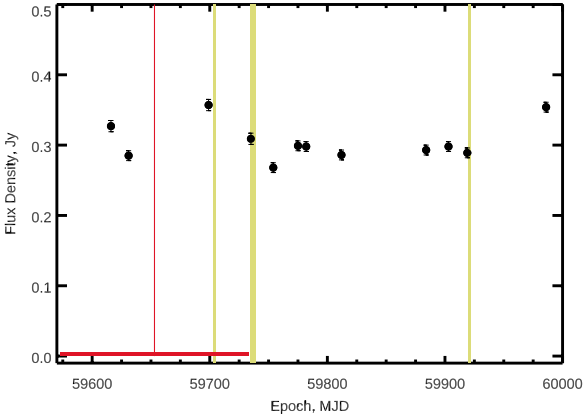

Fig. A.5: Polarization parameters of component $A0$ (black circles) and P (red circles): top panel - degree of polarization, bottom panel - position angle of polarization; the yellow areas mark *IXPE* observations, while blue triangles plot Π_X, and ψ_X; the dashed gray line in the bottom panel shows the direction of the jet according to Weaver et al. (2022), with dotted gray lines indicating its 1σ uncertainty.

Fig. A.4: Light curve of the core, $A0$; the red vertical line marks the time of the ejection of knot P, with its 1σ uncertainty indicated by the red horizontal line; yellow areas mark epochs of *IXPE* observations.

yellow areas, with the widest area covering two pointings (Obs. 2 and Obs. 3). Figure A.5 plots the values of Π_X and ψ_X, except during observations Obs. 2 & Obs. 3, when ψ_X rotated at a fast rate of ~85°/day (Di Gesu et al. 2023).

gree and angle, and (2) a rotating component with a constant polarization degree and a rotating polarization angle. The likelihood estimator for this model is:

$$S(\Pi_1, \Psi_1, \Pi_2, \Psi_2^0, R_1, \omega) =$$

$$- 2 \sum_i \ln\left[1 + \mu_i R_1 \Pi_1 \left(\cos 2\Psi_1 \cos 2\psi_i + \sin 2\Psi_1 \sin 2\psi_i \right) + \right.$$

$$\left. \mu_i(1 - R_1)\Pi_2 \left(\cos 2\Psi_2^0 \cos 2(\psi_i - \omega t) + \sin 2\Psi_2^0 \sin 2(\psi_i - \omega t) \right) \right] \quad \text{(B.1)}$$

where Π_1 and Ψ_1 are the polarization degree and angle of the constant component; Π_2 is the polarization degree of the rotating component, Ψ_2^0 is the initial polarization angle of the rotating component; ω is the rotation rate of the rotating component; R_1 is the relative intensity of the constant component; and μ_i is modulation factor of each event. We note that the fit with this model allows only extraction of the products of $R_1\Pi_1$ and of $(1 - R_1)\Pi_2$. The constant polarization model can be obtained from Equation B.1 by setting the ratio parameter to $R_1 = 1$. Similarly, the rotation model with constant polarization degree can be obtained by setting $R_1 = 0$.

Appendix B: Maximum likelihood method of multicomponent model

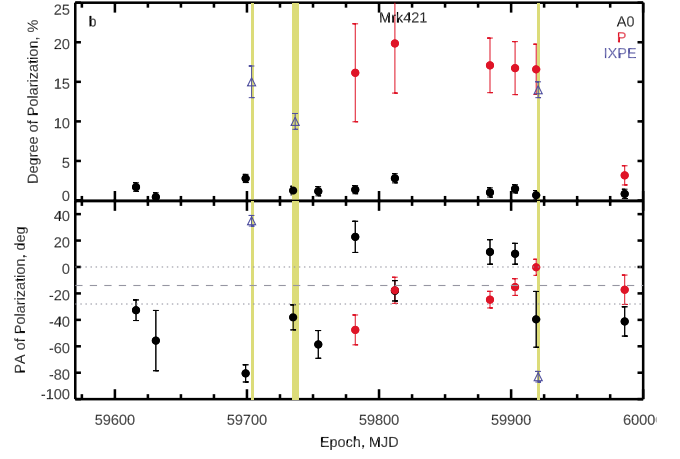The multicomponent model (Pacciani et al., in preparation) comprises (1) a constant component with a steady polarization de-